


**First operational dodecapole correction in the LHC**J. Dilly<sup>1,2,\*</sup> V. Ferrentino<sup>1,3</sup> M. Le Garrec<sup>1,4</sup> E. H. Maclean<sup>1</sup> L. Malina<sup>5</sup> T. Persson,<sup>1</sup>  
T. Pognat<sup>1</sup> L. van Riesen-Haupt<sup>6</sup> F. Soubelet<sup>1,7</sup> and R. Tomás<sup>1</sup><sup>1</sup>European Organization for Nuclear Research CERN, Geneva, Switzerland<sup>2</sup>Humboldt University of Berlin, Berlin, Germany<sup>3</sup>University of Naples Federico II, Naples, Italy<sup>4</sup>Goethe University Frankfurt, Frankfurt, Germany<sup>5</sup>Deutsches Elektronen-Synchrotron DESY, Notkestr. 85, 22607 Hamburg, Germany<sup>6</sup>Swiss Federal Institute of Technology Lausanne EPFL, Lausanne, Switzerland<sup>7</sup>University of Liverpool, Liverpool, United Kingdom (Received 22 January 2023; revised 6 October 2023; accepted 1 November 2023; published 5 December 2023)

Amplitude detuning measurements in the LHC have shown that a significant amount of detuning is generated via feed-down from high-order field errors in the magnets of the experiment insertion regions. This undesired effect can be detrimental to the luminosity production of the machine and is expected to be enhanced in the upcoming high-luminosity upgrade of the collider, the HL-LHC. In this study, we investigate the high-order errors in detail, performing amplitude detuning measurements during the commissioning of the LHC Run 3 and establish operational corrections via feed-down, using for the first time the dodecapole correctors in the insertion region.

DOI: [10.1103/PhysRevAccelBeams.26.121001](https://doi.org/10.1103/PhysRevAccelBeams.26.121001)**I. INTRODUCTION AND MOTIVATION**

Amplitude detuning, also known as “tune shift with amplitude,” describes the action-dependent tune shift in a storage ring and has significant impact on the tune footprint of the particle beams in the Large Hadron Collider (LHC), affecting dynamic aperture (DA) and beam lifetime [1,2]. It also influences the performance of beam instrumentation [2] and the control of Landau damping. Landau damping introduces a spread in synchrotron and betatron frequencies of individual particles within the beam, which suppresses collective unstable modes (e.g., head-tail instabilities), via dedicated octupole magnets (Landau Octupoles or MOs) in the arcs around the LHC [3,4].

To first order in field strength and first order in action, detuning is generated by normal octupole fields, weighted by powers of the  $\beta$  functions at the octupole sources [3,5] (see Sec. II C). Reduction of undesired detuning from octupole errors therefore directly relates to improved control of Landau damping, possibly reducing the necessary powering of the MOs.

It has been established, that in the LHC during proton-proton collisions, the main source of unwanted detuning

are normal octupole errors from the quadrupole triplets [2,4,6,7] left and right of the experimental insertions of ATLAS at Interaction Point (IP) 1 and CMS at IP5. The beam dynamics in the insertion regions (IRs) around the IP are very sensitive to errors, due to their high  $\beta$  functions, required to reach very small  $\beta^*$ , the value of the  $\beta$  function at the IP. Error correction in the IRs has therefore been subject to intensive studies during the design phase and in the actual machine, not only in the LHC [2,6–11], but in most synchrotron colliders, such as the Tevatron [12], RHIC [9,13], SuperKEKB [14] and in the Future Circular Collider [15–17]. One of the upgrades envisioned for the High-Luminosity LHC (HL-LHC) [18], are triplets with larger aperture, increasing the coil aperture from 70 mm in the LHC [4] to 150 mm. This allows for a doubling of the  $\beta$  function in the triplets, supporting  $\beta^*$  down to 15 cm [19] to raise collision rates and hence the name-giving high luminosity. Yet this change elevates the already high sensitivity to errors in this region [20,21]. The search and testing for suitable correction targets for increasingly higher field orders has been a long ongoing journey at the LHC [7,22–25].

The regions of the LHC housing the triplets are occupied by common-aperture magnets, meaning both circulating beams, named beam 1 and beam 2, share a single aperture between the so-called separation dipoles, which divide the beams again into their individual beam lines. The nonlinear correction packages [4] are located close to the triplets [2] within this region. A schematic of an IR of the LHC is given in Fig. 1. Any correction needs hence to be valid for both beams.

\*joschua.dilly@cern.ch

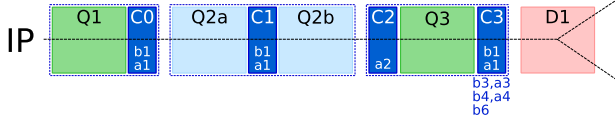


FIG. 1. Schematic of one side of a LHC IR region, showing the common-aperture magnets: Q1, Q2a/b, and Q3 are the triplet quadrupoles, C0-C3 the corrector packages with the field order to be corrected indicated (see Sec. II A). D1 is the separation dipole, diverging beam 1 and beam 2 to their respective beam lines. Blue lines mark common cryostats. The nonlinear corrector package, containing the dodecapole correctors, is included in C3.

One of the observables targeted to correct IR errors has been amplitude detuning. Amplitude detuning is a global parameter and therefore cannot display the individual contribution of each IP to the total detuning. To determine the origin of the errors, local orbit bumps have been introduced during measurements, generating feed-down (see Sec. II B) to tune and coupling which could then be mitigated using the octupole correctors within the nonlinear correction packages in each IR. Performing this correction has also led to immediate improvements in the performance of beam instrumentation, e.g., in the accuracy of the coupling measurement and the signal-to-noise ratio of the base-band tune (BBQ [26–28]) system [2].

During LHC commissioning in 2018, upon changing the crossing scheme from flat orbit to the operational scheme of locally closed orbit bumps in the IRs (see Table I), an increase in amplitude detuning was measured (see the summary in Table II in Sec. III or [29,30]). Further investigation [31] during machine development (MD) sessions confirmed this finding and revealed the main contribution to be feed-down from high-order errors, i.e., decapole and dodecapole errors and above, to the octupole fields, due to the crossing schemes in IP1 and IP5. While feed-down to tune from dodecapole fields induced by orbit bumps had been observed in other colliders [32], there have been no measurements of feed-down to first-order amplitude detuning outside of the LHC.

As the influence of the feed-down of magnetic fields depends on the (small) orbit offset raised to the power of the field’s order (see Sec. II B), field errors higher than dodecapole errors are ignored in the here presented study. Also sextupole errors and feed-down to them are omitted in the following discussion: not only are they less affected by feed-down from the high-order errors compared to octupole fields (see again Sec. II B), they also contribute only in second order in field strengths to amplitude detuning [5] and their correction has been discussed in, e.g., [2,6,34,35].

Dodecapole fields on the other hand are the first allowed harmonic of quadrupole magnets [36] and also contribute directly to second-order amplitude detuning (see Sec. II C). The harmful influence of decapole and dodecapole errors on dynamic aperture and beam lifetime in the upcoming

TABLE I. Machine settings used during measurements. Crossing is given in half-angles. The horizontal plane is X, the vertical plane is Y. MD3311 is the machine development session in 2018 [31] first investigating the feed-down from high-order errors, MD6863 the session in 2022 dedicated to dodecapole corrections.

TUNES:	$Q_x = 62.28,$		$Q_y = 60.31$		
EXCITATION:	[see Eq. (13)]				
2018	$\Delta_{Q_x} = -0.008,$		$\Delta_{Q_y} = 0.01$		
2022	$\Delta_{Q_{x/y}}^{\text{small}} = \mp 0.007,$		$\Delta_{Q_{x/y}}^{\text{big}} = \pm 0.009$		
OPTICS:	$\beta^* = 30$ cm round optics ( $\beta_x^* = \beta_y^*$ )				
<i>Commissioning</i>	April 28, 2018 <span style="float:right"><i>Full crossing</i></span>				
ENERGY:	6.5 TeV				
CROSSING:	IP-Plane	IP1-Y	IP2-Y	IP5-X	IP8-X
	$\mu\text{rad}$	160	200	160	-250
SEPARATION:	IP-Plane	IP1-X	IP2-X	IP5-Y	IP8-Y
	mm	-0.55	1.4	0.55	1.0
<i>MD3311</i>	June 16, 2018 <span style="float:right"><i>IP5 crossing</i></span>				
ENERGY:	6.5 TeV				
CROSSING:	IP-Plane			IP5-X	
	$\mu\text{rad}$			160	
SEPARATION	IP-Plane			IP5-Y	
& OFFSET:	mm			0.55  - 1.8	
<i>Commissioning</i>	May 9, 2022 <span style="float:right"><i>Full crossing</i></span>				
ENERGY:	6.8 TeV				
CROSSING:	IP-Plane	IP1-Y	IP2-Y	IP5-X	IP8-X
	$\mu\text{rad}$	-150	0	150	0
SEPARATION:	IP-Plane	IP1-X	IP2-X	IP5-Y	IP8-Y
	mm	0	0	0	0
<i>Commissioning</i>	June 4, 2022 <span style="float:right"><i>Full crossing</i></span>				
<i>&amp; MD6863</i>	June 24, 2022 <span style="float:right"><i>Full crossing</i></span>				
ENERGY:	6.8 TeV				
CROSSING:	IP-Plane	IP1-Y	IP2-Y	IP5-X	IP8-X
	$\mu\text{rad}$	-160	200	160	-200
SEPARATION:	IP-Plane	IP1-X	IP2-X	IP5-Y	IP8-Y
	mm	0	1.0	0	1.0
<i>MD6863</i>	June 24, 2022 <span style="float:right"><i>IP5 crossing</i></span>				
ENERGY:	6.8 TeV				
CROSSING:	IP-Plane	IP1-Y	IP2-Y	IP5-X	IP8-X
	$\mu\text{rad}$	0	200	$\pm 160$	-200
SEPARATION:	IP-Plane	IP1-X	IP2-X	IP5-Y	IP8-Y
	mm	0	1.0	0	1.0

HL-LHC has been shown in simulations and dedicated measurements, in which the normal dodecapole errors were artificially increased to replicate the HL-LHC conditions [25,37–41].

In this paper, detuning measurements are presented, which have been performed in 2022 during LHC commissioning and in a dedicated MD session (with the ID MD6863), confirming the observed errors still to be present in LHC Run 3. Important machine settings for these measurements are shown in Table I and a summary of the measured detuning terms can be found in Table II. A correction option, previously only researched in simulations [38], is explored: Normal dodecapole errors in the IRs are corrected using the observed change in amplitude detuning from feed-down, by in turn utilizing

the feed-down to normal octupoles from the dodecapole correctors in the nonlinear corrector packages of the IRs, which had been hitherto inactive during operation.

While measurements and corrections of magnetic fields up to dodecapole order, based on tune shifts using the feed-down artificially introduced by orbit bumps, had also been attempted at RHIC [32], these corrections were never (or only partially) used operationally, as they were detrimental to beam lifetime. On the other hand, a 4% increase of integrated luminosity was achieved using decapole and dodecapole correctors by targeting beam lifetime directly [42]. So while this is not the first time a particle collider uses dodecapole correctors operationally, it is the first time targeting the feed-down to amplitude detuning and hence also controlling Landau damping. For the LHC, this is in fact also the first time these correctors are used in operation.

This paper is structured as follows: In Sec. II, theoretical background, notations, and conventions are introduced, as well as the procedure for measurements, simulations, and corrections outlined. This is followed by the actual presentation and discussion of the results in Sec. III. Conclusions are drawn in Sec. IV, in which also outlook for further studies is suggested.

## II. BACKGROUND

### A. Field strengths

The multipole expansion of a general magnetic field  $\vec{B} = (B_x, B_y)$  in the planes  $x$  (horizontal) and  $y$  (vertical), into normal ( $B_n$ ) and skew ( $A_n$ ) field components of  $2n$  poles, reads

$$B_y + iB_x = \sum_{n=1}^{\infty} (B_n + iA_n)(x + iy)^{n-1}. \quad (1)$$

With Eq. (1), this paper follows the convention of using  $n = 1$  to indicate a dipole field. Extracting the main field component  $B_N$  of a normal  $2N$ -pole magnet, the expansion can be rewritten using  $b_n$  and  $a_n$  to represent normal and skew relative field errors at the reference radius  $R_{\text{ref}}$ :

$$B_y + iB_x = B_N \sum_{n=1}^{\infty} (b_n + ia_n) \left( \frac{x + iy}{R_{\text{ref}}} \right)^{n-1}, \quad (2)$$

and equivalently for  $A_N$ , the main field component of a skew  $2N$ -pole magnet.  $b_n$  and  $a_n$  are dimensionless but usually given in “units” of  $10^{-4}$ . As the correction described below makes use of normal dodecapole magnets and is mostly aimed at correcting the  $b_6$  error components (see Sec. III C), the shorthand “ $b_6$  correction” is employed in the figures and tables of this paper. The normal field component  $B_n$  of a normal  $2N$ -pole magnet is then

$$B_n [\text{Tm}^{1-n}] = B_N \times \frac{b_n}{R_{\text{ref}}^{n-1}} \quad (3)$$

and similar for skew field components  $A_n$ , as well as the skew and normal components of a skew  $2N$ -pole magnet.

It is customary to normalize the field strengths of Eq. (3) to the magnetic rigidity  $B\rho$ , defined by the main dipole field  $B$  of the accelerator and its bending radius  $\rho$ :

$$\begin{aligned} K_n [\text{m}^{-n}] &= \frac{B_n}{B\rho} (n-1)! \quad \text{and} \\ KS_n [\text{m}^{-n}] &= \frac{A_n}{B\rho} (n-1)!. \end{aligned} \quad (4)$$

### B. Feed-down

The effect of feed-down occurs when a particle beam’s orbit passes off-center through a magnet due to either a transverse misalignment of the magnet or an off-center closed orbit of the beam itself. In these cases, the magnetic field can be described as a composition of the current order main field plus lower order components and can be understood by applying a Taylor expansion on  $x$  and  $y$  in Eq. (1) or, equivalently, the Hamiltonian of the system in curvilinear (comoving) coordinates. These additional components therefore cause the same effects on the beam as lower order sources would [43]. Using Eqs. (1) and (4), and with  $(\Delta x, \Delta y)$  being the orbit of the off-center particle, feed-down to field order  $n \geq 1$  from fields up to order  $n + P$  can be expressed as

$$\begin{aligned} &(K_n + iKS_n)^{\text{w/feed-down}} \\ &= \sum_{p=0}^P (K_{n+p} + iKS_{n+p}) \frac{(\Delta x + i\Delta y)^p}{p!}. \end{aligned} \quad (5)$$

### C. Amplitude detuning from dodecapoles

Using the action  $J_u$ , the amplitude  $\mathcal{A}_u(s)$  of a particle in the transversal plane  $u \in \{x, y\}$  at longitudinal position  $s$  is

$$\mathcal{A}_u(s) = \sqrt{2J_u \beta_u(s)}. \quad (6)$$

The dependency of the tune on amplitude is usually given with respect to the invariant  $2J_u$  and is therefore location independent. The detuning coefficients can be expressed via Taylor expansion of the tune  $Q_u$  around the unperturbed tune at zero-action  $Q_{0u}$ ; explicitly stated up to second order in amplitude:

$$\begin{aligned} Q_u(2J_x, 2J_y) &= Q_{0u} + \frac{\partial Q_u}{\partial(2J_x)}(2J_x) + \frac{\partial Q_u}{\partial(2J_y)}(2J_y) \\ &+ \frac{1}{2!} \left( \frac{\partial^2 Q_u}{\partial(2J_x)^2}(2J_x)^2 \right. \\ &+ 2 \frac{\partial^2 Q_u}{\partial(2J_x)\partial(2J_y)}(2J_x)(2J_y) \\ &\left. + \frac{\partial^2 Q_u}{\partial(2J_y)^2}(2J_y)^2 \right) + \dots \end{aligned} \quad (7)$$

To numerically compute detuning integrals, a thin-lens approximation is used in which multipole elements are split into single kicks at  $s_w$  surrounded by drift spaces; the kick strength being  $K[S]_n L_w$ —the integrated strength  $K[S]_n(s)$  [see Eq. (4)] over the length  $L_w$  of element  $w$ .  $\beta$  function and orbit are then also approximated using the value at  $s_w$ . In this approximation, the contribution to the first-order terms of Eq. (7) from normal octupole fields of element  $w$  with integrated strength  $K_4 L_w$  can be calculated [44] as

$$\frac{\partial Q_x}{\partial(2J_x)} = \sum_w \frac{K_4 L_w}{32\pi} \beta_x^2(s_w) \quad (8a)$$

$$\frac{\partial Q_x}{\partial(2J_y)} = \frac{\partial Q_y}{\partial(2J_x)} = \sum_w -\frac{K_4 L_w}{16\pi} \beta_x(s_w) \beta_y(s_w) \quad (8b)$$

$$\frac{\partial Q_y}{\partial(2J_y)} = \sum_w \frac{K_4 L_w}{32\pi} \beta_y^2(s_w). \quad (8c)$$

Including feed-down, as in Eq. (5), from normal and skew decapoles ( $K_5 L$ ,  $KS_5 L$ ) and normal and skew dodecapoles ( $K_6 L$ ,  $KS_6 L$ ), we get due to the orbit  $\Delta x(s_w)$ ,  $\Delta y(s_w)$  at an element  $w$

$$\begin{aligned} & (K_4 L_w)^{w/\text{feed-down}} \\ &= K_4 L_w + \Delta x(s_w) K_5 L_w - \Delta y(s_w) K S_5 L_w \\ &+ \frac{1}{2} (\Delta x(s_w)^2 - \Delta y(s_w)^2) K_6 L_w - \Delta x(s_w) \Delta y(s_w) K S_6 L_w. \end{aligned} \quad (9)$$

Normal dodecapole magnetic fields also contribute directly and linearly to the second-order detuning terms of Eq. (7) in the following manner:

$$\frac{\partial^2 Q_x}{\partial(2J_x)^2} = \sum_w \frac{K_6 L_w}{384\pi} \beta_x^3(s_w) \quad (10a)$$

$$\frac{\partial^2 Q_y}{\partial(2J_x)^2} = \frac{\partial^2 Q_x}{\partial(2J_x) \partial(2J_y)} = \sum_w -\frac{K_6 L_w}{128\pi} \beta_x^2(s_w) \beta_y(s_w) \quad (10b)$$

$$\frac{\partial^2 Q_x}{\partial(2J_y)^2} = \frac{\partial^2 Q_y}{\partial(2J_x) \partial(2J_y)} = \sum_w \frac{K_6 L_w}{128\pi} \beta_x(s_w) \beta_y^2(s_w) \quad (10c)$$

$$\frac{\partial^2 Q_y}{\partial(2J_y)^2} = \sum_w -\frac{K_6 L_w}{384\pi} \beta_y^3(s_w). \quad (10d)$$

For brevity, in the following, we will use the symbols

$$Q_{a,b} = \frac{\partial Q_a}{\partial(2J_b)} \quad \text{and} \quad Q_{a,bc} = \frac{\partial^2 Q_a}{\partial(2J_b) \partial(2J_c)}, \quad (11)$$

as well as short hands for the coefficients

$$\tilde{\beta}_{a,b} = \begin{cases} \tilde{\beta}_{x,x} = \frac{\beta_x^2}{32\pi} \\ \tilde{\beta}_{x,y} = -\frac{\beta_x \beta_y}{16\pi} \\ \tilde{\beta}_{y,y} = \frac{\beta_y^2}{32\pi} \end{cases} \quad \text{and} \quad \tilde{\beta}_{a,bc} = \begin{cases} \tilde{\beta}_{x,xx} = \frac{\beta_x^3}{384\pi} \\ \tilde{\beta}_{x,xy} = -\frac{\beta_x^2 \beta_y}{128\pi} \\ \tilde{\beta}_{x,yy} = \frac{\beta_x \beta_y^2}{128\pi} \\ \tilde{\beta}_{y,yy} = -\frac{\beta_y^3}{384\pi} \end{cases}, \quad (12)$$

with  $a, b, c \in \{x, y\}$ .

## D. Measurements

### 1. Preparation

Before performing the measurements at each new machine configuration, global coupling between the transversal planes is manually corrected to  $|C^-| \leq 10^{-3}$  [45], to avoid detrimental effects on the amplitude detuning measurements [46]. This standard procedure, which is minimizing the coupling resonance driving terms (RDTs)  $f_{1001}$  [47], has been established for the LHC from Run 1 [48] and has been improved over the years [45,49–52].

Orbit stability is achieved due to the automatic orbit-feedback system in the LHC [53]. This system ensures that the orbit stays close to the reference orbit from the model within a root-mean-square deviation of  $\leq 70 \mu\text{m}$  [54] on an orbit of 5 to 8 mm at triplets and correctors when the crossing scheme is enabled.

### 2. Detuning

While in the beginning of LHC operation, amplitude detuning has been measured based on free oscillations following a single dipole “kick” [55], in later years, they were achieved using forced oscillations with an ac dipole [33,56,57]. Optics measurements with ac dipoles had already been tested at RHIC [58,59], and in the SPS in preparation for LHC optics measurements [60–62].

The oscillations, close to the tune frequency, are adiabatically ramped up and down to and from the desired amplitude [33,63,64]. Exciting single pilot bunches ( $\approx 10^{10}$  protons) per beam, this method allows for measurements at top energy without endangering machine safety and without beam decoherence or emittance growth. This means, a single bunch can be excited multiple times without having to go through the time-consuming process of dumping the blown-up beam, ramping down the magnets to injection settings, refilling the proton bunches, ramping to top energy again and performing the optics squeeze (i.e., the reduction of  $\beta^*$  to the desired value). The transverse positions of the beam centroid over approximately 6600 turns are captured during the ac dipole’s flattop at each beam position monitor [65] and then analyzed. Due to the use of the ac dipole, the first-order amplitude detuning direct terms  $Q_{x,x}$  [Eq. (8)] and  $Q_{y,y}$  [Eq. (8c)] will be enhanced by a factor of 2, while the second-order direct terms  $Q_{x,xx}$

[Eq. (10)] and  $Q_{y,yy}$  [Eq. (10d)] are enhanced by a factor of 3 [33]. All detuning data presented in this paper are compensated for these factors and detuning terms quoted are the “free” detuning of the machine. In principle, also the second-order terms  $Q_{x,xy}$  and  $Q_{y,xy}$  are doubled during forced oscillations, yet only the tune shift with the action of one plane has been measured during the study presented here and these terms have therefore not been investigated.

ac dipole excitations are generally performed in two transverse planes at the same time to be able to measure both tunes. The amplitude of one plane is kept low and constant, while slowly increasing the strength, i.e., action, of the other plane. During the measurements of 2018, the tune differences

$$\Delta_{Q_u} = |Q_u - Q_u^{\text{ac}}| \quad (13)$$

between the “natural” tune  $Q_u$  of the machine and the driven tune  $Q_u^{\text{ac}}$  induced by the ac dipole were fixed per plane to  $\Delta_{Q_x} = -0.008$  and  $\Delta_{Q_y} = 0.01$ . In 2022, an improved strategy was employed to enhance measurement quality: while still keeping the asymmetry  $\Delta_{Q_x} \neq \Delta_{Q_y}$  between the two planes to avoid exciting diagonal resonances [66,67], a smaller  $\Delta_{Q_u}^{\text{small}} = \mp 0.007$  was applied to the plane in which the kick amplitude was kept low, in contrast to the slightly larger  $\Delta_{Q_u}^{\text{big}} = \pm 0.009$  of the other plane. This was done to ensure good quality measurements even at the low amplitudes by having a boosted signal strength of the tune line due to the decreased adiabaticity of the excitation ramp. The amplitude is increased within the amplitude range of the ac dipole only in small steps and only until first losses at the collimators can be seen, to not risk a beam dump and to not lose beam intensity, needed to ensure good signals in the subsequent measurements. To achieve a good measurement, 10–15 kicks going beyond  $2J = 15$  nm is desirable, yet in configurations where the kick aperture was limited, kicks up to only  $2J = 5$  nm have yielded still usable results. When the available kick amplitude has been exploited, the procedure is repeated with the roles of the planes switched.

### E. Data analysis

The resulting turn-by-turn data are then processed by in-house PYTHON software tools [68]: Cleaning is done automatically via a specialized singular-value-decomposition (SVD) and Fourier transform on the signal [69,70], followed by a combination of automated and manual cleaning steps to remove faulty BPMs and ascertain the correct tune line in the spectrum [71], an example of which is shown in Fig. 2.

In preparation for extensive amplitude detuning studies like the one presented, these latter methods have recently been extended with new features, such as automated BPM cleaning (via the *Outlier Filter* described below) and an option for manual spectral-line selection. This has allowed for fast online (i.e., during measurements) analysis of the

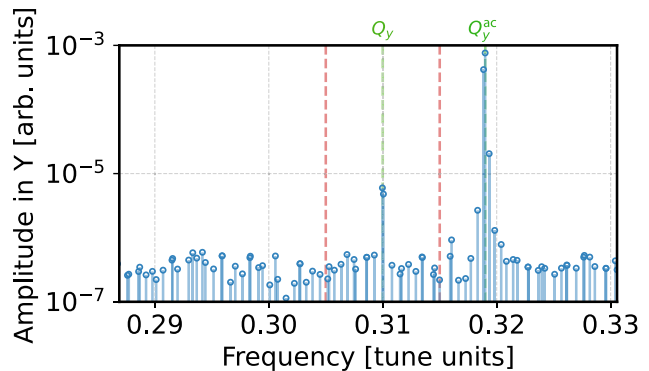


FIG. 2. Example for measured spectrum at a single BPM in the vertical plane. The frequency range around the natural ( $Q_y$ ) and driven ( $Q_y^{\text{ac}}$ ) vertical tunes is shown. The dashed lines in red indicate the set window, in between which the highest peak is considered to be the natural tune.

data during the MD, which had not been possible to this level in the past.

#### 1. Outlier filter

The outlier filtering function [69] is utilized at multiple stages of the data analysis and operates in the following way: The function gets an array  $x$  of data of length  $n_x$ , which can be any scalar data but in the context of this paper has been data of the tunes, either measured per BPM or a time series from the BBQ. It removes data points in the tails of the measured distribution, which are too populated assuming  $x_n$  to be samples from a normal distribution, specified by measured mean and standard deviation of the given data, due to the finite sample size  $n_x$ . A data point, outside of a user-specified limit, is removed if its two-sided  $p$  value is smaller than  $1/n_x$ , given the t-distribution defined by the measured samples. For 500 BPMs, for example, this translates to a cutoff at  $\approx 3.1\sigma$ . This filtering method is first applied to filter out BPMs for which the driven or natural tunes were not correctly identified and later to clean the tune data from the BBQ, used to establish the baseline for the machine tune at zero action (see Sec. II E).

#### 2. Action

The action  $2J$  is calculated at each BPM at location  $s$  from the amplitude  $\mathcal{A}_{\text{BPM}}$  of the main line of the BPM spectrum (i.e., the driven tune  $Q^{\text{ac}}$  line, as in Fig. 2) via

$$2J_{\text{BPM}} = \frac{\mathcal{A}_{\text{BPM}}^2}{\beta_{\text{model}}(s)}. \quad (14)$$

Instead of the  $\beta$  function from the model (as in [72]), the measured  $\beta$  values can also be used as shown in [73], yet this feature has not yet been implemented in the analysis code. Due to the low  $\beta$  beating in the machine [74,75], with a root-mean-square beating of  $<2\%$  [75], the use of the model  $\beta$  function is still justified.

The action is further rescaled to perform beam-based adjustments for residual BPM calibration errors [73], by the mean ratio of the  $\beta$  function estimated from phases [76] and the  $\beta$  function from amplitudes [72] at the arc BPMs per kick.

The error on the action  $\delta 2J_{\text{BPM}}$  can be acquired from the error on the amplitude  $\delta \mathcal{A}_{\text{BPM}}$ , which in turn is estimated from the noise on the signal:

$$\delta \mathcal{A}_{\text{BPM}} = \sqrt{\frac{2}{N_{\text{Turns}}}} R_{\text{BPM}}^{(\text{cleaned})}. \quad (15)$$

$N_{\text{Turns}}$  is the number of turns over which the measurement is recorded and  $R_{\text{BPM}}^{(\text{cleaned})}$  is the estimated BPM resolution of the cleaned signal. Here, BPM resolution is defined as the standard deviation of the noise, which is first estimated by the difference between the cleaned signal and the original signal at the BPM (as  $R_{\text{BPM}}^{(\text{raw})}$ ). On this estimate, a coefficient has been matched via an empirical study, targeting, e.g., the ratio of the noise floor levels in the frequency spectra of raw data and SVD-cleaned data:

$$R_{\text{BPM}}^{(\text{cleaned})} = \frac{1}{\sqrt{2} \times 10} R_{\text{BPM}}^{(\text{raw})}. \quad (16)$$

With Eqs. (14) and (15), we can calculate the error on the action:

$$\delta 2J_{\text{BPM}} = \frac{2\mathcal{A}_{\text{BPM}}\delta \mathcal{A}_{\text{BPM}}}{\beta_{\text{model}}(s)}. \quad (17)$$

From these estimates at each BPM for actions  $2J_{\text{BPM}_s} = \{2J_{\text{BPM}_1}, \dots, 2J_{\text{BPM}_N}\}$  and corresponding errors  $\delta 2J_{\text{BPM}_s} = \{\delta 2J_{\text{BPM}_1}, \dots, \delta 2J_{\text{BPM}_N}\}$ , we want to get an estimate for the actual action and the error we might be making on this estimation.

We can use inverse-variance weighting to define an error-weighted average of a set of measurements  $x = \{x_1, \dots, x_N\}$  and their associated errors  $\delta x = \{\delta x_1, \dots, \delta x_N\}$

$$\langle x \rangle_\delta = \frac{1}{\sum_{n=1}^N \frac{1}{\delta x_n^2}} \sum_{n=1}^N \frac{x_n}{\delta x_n^2} = \frac{1}{S_\delta(x)} \sum_{n=1}^N \frac{x_n}{\delta x_n^2}, \quad (18)$$

defining also a sum-of-weights  $S_\delta(x)$ . Equation (18) is used to get an estimate of the action in the machine:

$$2J = \langle 2J_{\text{BPM}_s} \rangle_\delta. \quad (19)$$

For the estimation of the error on this quantity, we can calculate the error-weighted variance on the data

$$\sigma_\delta^2(x) = \left\langle |x - \langle x \rangle_\delta|^2 \right\rangle_\delta \quad (20)$$

as well as the variance on  $\langle x \rangle_\delta$  itself:

$$\sigma^2(\langle x \rangle_\delta) = \frac{1}{\sum_{n=1}^N \frac{1}{\delta x_n^2}} = \frac{1}{S_\delta(x)}, \quad (21)$$

and the effective sample size

$$N_\delta(x) = \frac{(\sum_{n=1}^N \frac{1}{\delta x_n^2})^2}{\sum_{n=1}^N (1/\delta x_n^2)^2}. \quad (22)$$

Also using the abbreviations  $\sigma_\delta^2 = \sigma_\delta^2(2J_{\text{BPM}_s})$ ,  $N_\delta = N_\delta(2J_{\text{BPM}_s})$ , and  $S_\delta = S_\delta(2J_{\text{BPM}_s})$ , the error on the action can then be estimated via the unbiased sum of the two above described variances:

$$\delta 2J_{\text{estimated}} = \sqrt{\frac{N_\delta}{N_\delta - 1} \left( \sigma_\delta^2 + \frac{1}{S_\delta} \right)}. \quad (23)$$

To account for the measurement's finite sample size, while still estimating the standard deviation of a normally distributed quantity (student's t distribution with an infinite number of degrees of freedom), the error value is corrected by a multiplicative coefficient. We calculate the coefficient  $t_{\text{correction}}$  utilizing the cumulative distribution function  $F(s, N)$  of student's t distribution (with mean equal to 0 and spread equal to 1) as a function of the actual value  $s$  and the number of degrees of freedom  $N$ :

$$t_{\text{correction}} = F^{-1}(F(1, \infty), N_\delta), \quad (24)$$

which is a factor toward the limiting case  $N \rightarrow \infty$  for a given confidence level corresponding to  $1\sigma$  in the normal distribution.

$$\delta 2J = \delta 2J_{\text{estimated}} \times t_{\text{correction}}. \quad (25)$$

These statistical functions are part of the OMC3 package [68]. The calculations are done individually for each transversal plane.

### 3. Tune

As shown in Fig. 2, for each BPM, the natural tune is identified within a given frequency window as the line with the largest amplitude in that window [70]. Again, the two transversal planes are handled identically and separately. The selected lines are manually confirmed in a spectral plot and can be modified if needed.

The measured natural tune  $Q_u$  and its error  $\delta Q_u$  at the time of the excitation are calculated from the selected spectral lines by the mean and standard deviation over the BPMs, after cleaning as described at the beginning of this section. The natural tune at zero action [ $Q_{0u}$  in Eq. (7)] is found around each excitation time from the BBQ data logged in the LHC, which removes the influence of

possible tune drifts during the measurement duration. The BBQ data are first cleaned using a sliding window of 100 data points, which translates to roughly 15 s of data, and applying the *Outlier Filter* described above within each window. This removes measurement outliers of the BBQ as well as the excited tunes during the ac-dipole operation, which lasts about 1 s. If a value is removed in any window, it will be completely excluded from analysis. From this filtered data, the mean is calculated for each window, resulting in a moving average. This average is in turn subtracted from the data points to calculate a moving standard deviation using the same window lengths. The tunes  $Q_{0u}$  are then the value of the moving average closest to the kick times, while the error on those measurements  $\delta Q_{0u}$  are the values of the moving standard deviation at the same times. The tune values for the detuning fit are then

$$\Delta Q_u = Q_u - Q_{0u} \quad (26)$$

$$\delta \Delta Q_u = \sqrt{\delta Q_u^2 + \delta Q_{0u}^2}. \quad (27)$$

#### 4. Fitting

To get the first-order detuning coefficients, the slope of the detuning  $\Delta Q$  over the actions  $2J$  at different kick amplitudes and their errors  $\delta \Delta Q$  and  $\delta 2J$  is fitted to a linear polynomial by means of an orthogonal distance regression (ODR) algorithm [77] provided by the `scipy` python package [78]. ODR also produces an estimated error (one standard deviation) on the fit. In principle, also a fit to second-order polynomials is possible, yet, as will be discussed in Sec. III D, due to the low kick amplitudes in most of the measurements, no usable fits could be obtained.

Examples of the results of the measurement at different crossing angles are given in Fig. 3: In this figure, the data points show the measured shift in tune in the vertical plane from the machine tune  $\Delta Q_y$  [Eq. (26)] at the  $2J_y$  of the performed kicks [Eq. (19)]. The detuning coefficient  $Q_{y,y}$  is then slope of the linear ODR fit on these data points. Depicted is the data of beam 2 of four different scenarios, all without dodecapole correction, as performed during the MD in 2022.

The fit values and their standard deviation for all relevant measurement scenarios can be found in Table II: the measurement results from 2018 which triggered the study, and from commissioning and the MD in 2022. A discussion of the data is presented in Sec. III.

#### F. Correction approach

The normal dodecapole corrector elements (MCTX) left and right of IP1 and IP5 are used to compensate for the measured detuning change  $\Delta Q_{a,b}$  with application of the crossing angle. As the contributions to detuning add up

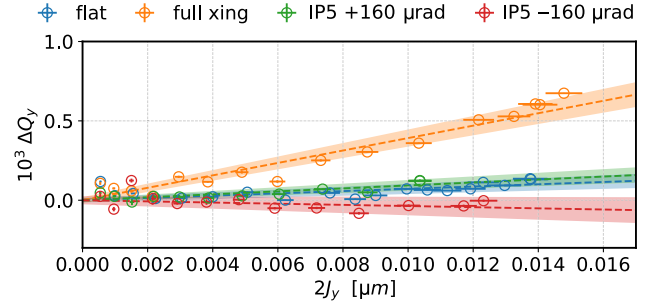


FIG. 3. Data of the measured vertical detuning of multiple kicks at increasing vertical action in beam 2. This is the data of the measurement without dodecapole correction from MD6863 (Table I). Dashed lines show the linear fit to the data points, while the colored area covers one standard deviation of the fit. The constant part of each fit has been subtracted for plotting from the fit and its respective data points. Shown are the scenarios of flat orbit (blue), with full crossing scheme applied (orange), and with crossing only in IP5 at +160  $\mu\text{rad}$  (green) and  $-160 \mu\text{Rad}$  (red). These are examples of the measurements of four data points in Table II, presented and discussed in Sec. III.

linearly, an equation system can be built with these correctors as unknowns, targeting  $-\Delta Q_{a,b}$ :

$$\begin{aligned} & - \begin{pmatrix} \Delta Q_{a,b}^{(B1)} \\ \Delta Q_{a,b}^{(B2)} \\ \vdots \end{pmatrix} \\ & = \begin{pmatrix} M_{a,b;L1}^{(B1)} & M_{a,b;R1}^{(B1)} & M_{a,b;L5}^{(B1)} & M_{a,b;R5}^{(B1)} \\ M_{a,b;L1}^{(B2)} & M_{a,b;R1}^{(B2)} & M_{a,b;L5}^{(B2)} & M_{a,b;R5}^{(B2)} \\ \vdots & \vdots & \vdots & \vdots \end{pmatrix} \cdot \begin{pmatrix} K_6 L_{L1} \\ K_6 L_{R1} \\ K_6 L_{L5} \\ K_6 L_{R5} \end{pmatrix}, \end{aligned} \quad (28)$$

where the matrix elements are the detuning coefficients from Eq. (12) with feed-down from  $K_6$  to  $K_4$  [see Eq. (9)]

$$M_{a,b;w}^{(BN)} = \frac{1}{2} (\Delta x_w^{(BN)^2} - \Delta y_w^{(BN)^2}) \tilde{\beta}_{a,b;w}^{(BN)}, \quad (29)$$

using the subscript short-hands  $LIP, RIP$  for the corrector elements left and right of  $IP \in \{1, 5\}$ .  $BN \in \{B1, B2\}$  indicates the beam. Equation (28) can be extended, as hinted at by the vertical dots, to include multiple targeted detuning terms  $\Delta Q_{a,b}$ , as well as different setups, e.g., the same detuning term but with different crossing angles. The resulting equation system can then be solved, or the error on the solution minimized, by standard linear optimizers.

Before the data of 2022 could be measured, more complex scenarios were studied using the 2018 data presented in [79], e.g., targeting single IRs or using inequalities. This was done to account for the noisy

measurement of some terms while still trying to enforce desired trends, e.g., forcing terms to be positive after correction. In 2022, due to the improvement of data quality, these complex scenarios were put aside and all corrections are based on solving Eq. (28), targeting equality to the measured detuning shifts  $\Delta Q_{a,b}$ . During commissioning and the MD, the measured changes in detuning were exclusively based on the difference between flat orbit and with crossing in both IR1 and IR5 (see Table I), due to the data from single IRs not yet being available at the time of the “online” correction calculations. These corrections could be tested and verified in the machine. After the data from the measurements with individual crossing schemes in IR5 (again Table I) had been analyzed, corrections were also calculated taking these into account and are discussed in Sec. III C.

### G. Correction calculation

In simulations, the nominal LHC is recreated in CPYMAD [80], a python wrapper for MAD-X [81], using the Run 3 sequence and  $\beta^* = 30$  cm round optics. There are no errors included into the model. The orbit is set up according to the desired realization, as described in Table I.

From the optics functions, acquired using the TWISS command in MAD-X, and the measurement data, the desired equation systems of Eq. (28) are built and a sum-of-squares minimization performed using the (Moore-Penrose) pseudoinverse of the matrix build from  $M_{a,b,w}$  derived from the model. The uncertainties on the measurement fits  $\Delta Q_{a,b}$  are propagated to the resulting corrections. At this point, it would be possible to introduce weights for the different detuning terms, to increase or reduce the importance of a term, as has been partially done in simulation in [79], e.g., to support the Landau damping strategy. For the current study, no such weighting was applied, as we wanted to minimize the detuning in its entirety: On one hand, the detuning introduced from the Landau octupoles is independent of crossing angle and hence introducing an orbit-dependent component is not desirable, on the other hand, the detuning is used in this study as an accessible observable to attempt the correction of dodecapole field errors as locally as possible to also reduce their other impacts on the machine optics, such as second-order detuning and driving of resonances. In addition, this study is also performed in preparation for HL-LHC commissioning, for which the polarity of the Landau octupoles, and therefore the detuning terms which need to be targeted, has not been decided yet [82].

To check the validity of the calculations, the obtained corrector strengths are applied to the simulated lattice and the actual detuning change is determined from the PTC-module [83,84] as well as from Eqs. (8) and (9).

The corrections can then be trimmed into the accelerator via the LHC Software Architecture (LSA [85]) and their actual effectiveness evaluated.

## III. RESULTS

### A. Detuning measurements

During the 2022 LHC commissioning and again for verification and improvement during MD, measurements were performed at the top-energy of LHC Run 3 of 6.8 TeV, after squeezing the beam to  $\beta^* = 30$  cm.

The data were evaluated following the procedure described in Sec. II D. The errors on the detuning fit were, especially for kicks with large amplitude, dominated by the errors on the action  $\delta 2J$  [Eq. (25)], which were typically of the order of 6% of  $2J$ . The error on the tune was usually smaller, with on average an absolute error on the measured natural tune  $\delta Q_u$  of  $3 \times 10^{-5}$ , which in turn dominated the error on the tune shift  $\delta \Delta Q_u$  [Eq. (27)], as the error  $\delta Q_{0u}$  from the BBQ was an order of magnitude lower. The final detuning fits of these measurements are listed in Table II.

During MD, detuning without dodecapole corrections (“w/o  $b_6$ ”) was probed at multiple crossing angle settings, i.e., at flat orbit, with crossing in IP1 and IP5 and with crossing in IP5 only, but at two opposite crossing angle values. This was done to not only measure the detuning change but also determine its origin in location and field order, as will be discussed in detail below.

Despite similar machine settings at flat orbit and with the full crossing scheme in place (see Table I), differences could be seen in the detuning measurements from different dates in 2022. Between measurements, various corrections had been applied to the LHC, which are named in the caption of Fig. 4. Yet, the expected detuning changes from these do not seem to replicate the observed differences, as demonstrated for the flat-orbit measurements in Fig. 4.

In contrast to the results in 2018, large cross-term detuning is present in beam 1 even at flat orbit (see Table II). The sources of it have not yet been identified and the discovery is surprising, as between LHC Run 1 and Run 2, the octupole errors had not changed, and in both here presented cases, 2018 and 2022, corrections up to octupole order had been implemented beforehand. These findings have been presented to the LHC Machine Committee (LMC) [87].

### B. Dodecapole corrections

Detuning measurements were carried out first at flat orbit and then with the full crossing scheme applied, to establish the change in detuning between the two scenarios. Following Secs. II F and II G, normal dodecapole corrections were calculated from the resulting detuning differences, which were then in turn verified by repeating the measurements with powered dodecapole correctors. As an example, the measurement of the direct horizontal term of beam 2 during commissioning is shown in Fig. 5: The figure illustrates the detuning change  $\Delta Q_{a,b}$ , the difference between the detuning terms  $Q_{a,b}$  between different scenarios, in particular, the detuning change of a scenario with crossing scheme and flat orbit. In this instance, it can be seen that



TABLE II. Summary of amplitude detuning measurements from 2018 [29–31] at 6.5 TeV and  $\beta^* = 0.3$  m and 2022 at 6.8 TeV and  $\beta^* = 0.3$  m. Detailed orbit setups are described in Table I while here the measurements are identified by either “flat orbit” (i.e., crossing bumps deactivated) or which of IP1 and IP5 are activated and at (“@”) which half-angle. If both IPs are mentioned with different signs, the top sign refers to IP1 and the bottom sign to IP5. The four detuning terms are abbreviated as in Eq. (11):  $Q_{a,b} = \partial Q_a / \partial (2J_b)$ . Results for beam 1 are shown in the top row and for beam 2 in the bottom row for each measurement. Where ac-dipole kicks were used, the results have been corrected for the effect of forced oscillations [33].

		$Q_{x,x}$ ( $10^3\text{m}^{-1}$ )	$Q_{y,x}$ ( $10^3\text{m}^{-1}$ )	$Q_{x,y}$ ( $10^3\text{m}^{-1}$ )	$Q_{y,y}$ ( $10^3\text{m}^{-1}$ )
2018	Commissioning	$34 \pm 1$	$8 \pm 2$	$18 \pm 1$	$-38 \pm 1$
	IP1 & 5@ + 160 $\mu\text{rad}$	$-3 \pm 1$	$-10 \pm 3$	$-14 \pm 2$	$13 \pm 3$
	MD3311	$0.8 \pm 0.5$	$10 \pm 1$	$6 \pm 2$	$20 \pm 5$
	Flat orbit	$-7.5 \pm 0.5$	$8 \pm 2$	$-2 \pm 1$	$6 \pm 1$
	MD3311	$56 \pm 6$	$-9 \pm 15$	$-78 \pm 7$	$2.5 \pm 0.8$
	IP5@ + 160 $\mu\text{rad}$	$1.5 \pm 0.5$	$4 \pm 1$	$-4 \pm 3$	$12 \pm 1$
2022	Commissioning w/o $b_6$	$-15.4 \pm 0.9$	$32.2 \pm 2$	$33.7 \pm 1.0$	$-8.4 \pm 0.5$
	Flat orbit	$-8.7 \pm 0.7$	$13 \pm 2$	$-3 \pm 2$	$10 \pm 0.9$
	Commissioning w/o $b_6$	$20 \pm 4$	$43 \pm 4$	$33 \pm 10$	$-10 \pm 3$
	IP1 & 5@ $\mp$ 150 $\mu\text{rad}$	$26 \pm 0.8$	$-31 \pm 3$	$-27 \pm 4$	$18 \pm 7$
	Commissioning w/ $b_6$	$-34 \pm 7$	$38 \pm 3$	$24 \pm 4$	$-6 \pm 1$
	Flat orbit	$-15 \pm 2$	$10 \pm 3$	$6.3 \pm 0.4$	$-3.6 \pm 0.6$
	Commissioning w/ $b_6$	$-21 \pm 4$	$47 \pm 2$	$56 \pm 6$	$15 \pm 1$
	IP1 & 5@ $\mp$ 160 $\mu\text{rad}$	$-28 \pm 2$	$22 \pm 4$	$13 \pm 2$	$-7.8 \pm 0.5$
	MD6863 w/o $b_6$	$-18 \pm 2$	$32 \pm 2$	$22 \pm 4$	$-0.0 \pm 0.9$
	Flat orbit	$-19.2 \pm 1.7$	$13.1 \pm 1.7$	$12 \pm 2$	$3.4 \pm 0.8$
	MD6863 w/o $b_6$	$9 \pm 2$	$36.8 \pm 2.0$	$27 \pm 2$	$2.1 \pm 1.0$
	IP1 & 5@ $\mp$ 160 $\mu\text{rad}$	$20.9 \pm 1.1$	$-39 \pm 2$	$-42.7 \pm 1.6$	$19.7 \pm 1.3$
	MD6863 w/o $b_6$	$23 \pm 2$	$1 \pm 2$	$-3.7 \pm 1.2$	$3.0 \pm 1.4$
	IP5@ + 160 $\mu\text{rad}$	$10.6 \pm 1.2$	$-8 \pm 3$	$-15.8 \pm 1.6$	$5.3 \pm 1.2$
	MD6863 w/o $b_6$	$8.9 \pm 1.4$	$4 \pm 3$	$-0.9 \pm 0.5$	$0.3 \pm 0.5$
IP5@ - 160 $\mu\text{rad}$	$20.3 \pm 1.7$	$-15 \pm 4$	$-23.3 \pm 1.7$	$-1.5 \pm 1.6$	
MD6863 w/ $b_6$	$-12.7 \pm 1.0$	$33 \pm 2$	$30.1 \pm 1.0$	$17.5 \pm 1.4$	
IP1 & 5@ $\mp$ 160 $\mu\text{rad}$	$-46 \pm 4$	$31 \pm 2$	$34.5 \pm 1.4$	$-17.9 \pm 1.0$	

the difference  $\Delta Q_{x,x}$  between flat orbit (blue) and with crossing angles and dodecapole corrections applied (green) has been severely reduced over the detuning change between flat orbit (blue) and with crossing angles but without

dodecapole corrections (orange). In the figures discussed below (Figs. 6, 7, and 10–12), only these detuning differences  $\Delta Q_{a,b}$  are shown to illustrate the effectiveness of the corrections. In the legend and on the  $x$  axes of the following

TABLE III. Dodecapole-corrector strength values ( $K_6$ ). In parenthesis, the percentage of the maximum powering at 6.8 TeV is given. The “w/ IP5” and “w/o IP5” labels on the MD6863 corrections refer to whether the additional measurements of crossing-bumps only around IP5 were taken into account or not (see Section III C). Below also the  $\beta$  functions at the correctors are given, rounded to meters. The  $\beta$  symmetries are accurate to below 10 cm.

	IP1		IP5	
	MCTX. 3L1 ( $10^3 \text{ m}^{-6}$ )	MCTX. 3R1 ( $10^3 \text{ m}^{-6}$ )	MCTX. 3L5 ( $10^3 \text{ m}^{-6}$ )	MCTX. 3R5 ( $10^3 \text{ m}^{-6}$ )
Commissioning 2022	$-0.606 \pm 715$ (2%)	$-2.696 \pm 1.179$ (7%)	$5.004 \pm 752$ (14%)	$-5.053 \pm 907$ (14%)
MD6863 w/o IP5	$1.269 \pm 731$ (3%)	$-3.288 \pm 577$ (9%)	$6.367 \pm 563$ (18%)	$-4.087 \pm 782$ (11%)
MD6863 w/ IP5	$0.493 \pm 192$ (1%)	$-3.982 \pm 188$ (11%)	$5.003 \pm 132$ (14%)	$-5.032 \pm 162$ (14%)
$\beta_x^{(B1)}$ and $\beta_y^{(B2)}$	3494 m	7177 m	3494 m	7177 m
$\beta_y^{(B1)}$ and $\beta_x^{(B2)}$	7177 m	3494 m	7177 m	3494 m

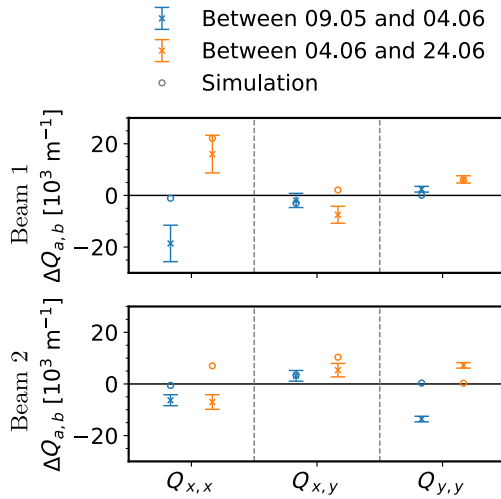


FIG. 4. Differences of detuning at flat orbit in measurement (crosses and error bars) between the first two measurements (orange) and between the second and third measurement (blue) in 2022 compared to the simulated expected changes from differences in LHC machine settings (circles), using the calculated corrections of “MD6863 w/ IP5” in Table III (with opposite signs) as error sources. The differences between the 09.05 and 04.06 were crossing schemes in IP2 and IP8, skew and normal sextupole corrections in IP1 and IP5, as well as the “commissioning 2022” correction, which was active at the time of the second measurement. Between 04.06 and 24.06, the dodecapole correction was deactivated again, but local corrections in the first single-aperture quadrupole (Q4) of beam 2, corrections of arc 81 and arc 45 in beam 1, and global  $\beta$  beating and dispersion corrections for each beam, were applied. Additionally, a waist-shift correction had been applied in beam 2 at IP5 [86].

figures,  $Q_{a,b}$  is used as a short hand to label the respective detuning term.

During commissioning, the measurements were done on two separate occasions, allowing for “offline” analysis of the results, while during the MD, the analysis and calculation of corrections were done “online,” that is during the measurement period. As the two first-order cross terms [Eq. (8b)] are referring to the same physical quantity, only one value was used in the corrections to give all three detuning terms [Eq. (8)] equal weight. For the corrections during commissioning, these values were picked from one of the measurements, based on the quality of the measured data: At flat orbit, the measured value (Table II) of  $Q_{x,y}$  was used for beam 1 and the value of  $Q_{y,x}$  for beam 2. With crossing enabled  $Q_{y,x}$  for beam 1 and  $Q_{x,y}$  beam 2 were used. During the MD, a different approach was elected and the average of the measured values  $Q_{x,y}$  and  $Q_{y,x}$  was designated as correction target. The latter approach is also used in the figures of this chapter, when only one cross term is mentioned (i.e., Figs. 6,7, and 10–12).

The calculated corrective powering of the dodecapole magnets is presented in Table III, including estimated errors on the correction from the errors on the fits of the

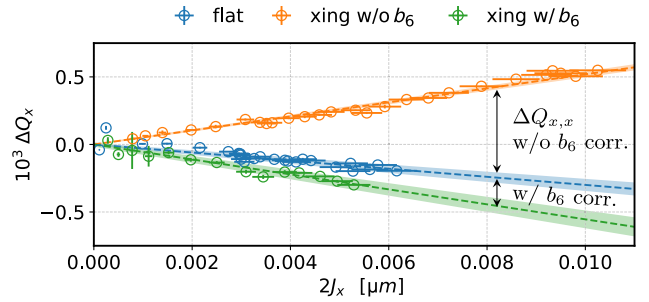


FIG. 5. Data of the measured direct horizontal detuning term in beam 2 during commissioning in 2022. The data points are presented in the same way as discussed for Fig. 3 in its caption and in Sec. II E: The shift in tune from the natural tune  $\Delta Q_x$  is shown as a function of the action of the kicks. Shown are the scenarios of flat orbit (blue), with full crossing scheme applied without dodecapole correction (orange), and with full crossing scheme applied with the “Commissioning 2022” dodecapole correction from Table III (green). Dashed lines show the linear fit to the data points, while the colored area covers one standard deviation of the fit. The detuning  $Q_{x,x}$  is then the slope of this fit and can be found in Table II. The constant part of each fit has been subtracted for plotting from the fit and its respective data points. The black arrows indicate the detuning change  $\Delta Q_{x,x}$ , i.e., the difference in  $Q_{x,x}$  between each of the two “with crossing” scenarios and flat orbit.

measurement and also including the percentage of the maximum absolute powering of the magnets. We can see, that the corrections calculated in commissioning have almost equal powering between left and right in IR5 at 14% of the maximum strength. There is a stronger powering in IR5 compared to IR1, where a maximum of only 7% is reached in the right corrector. The corrections from the MD (“MD6863 w/o IP5”) are in general slightly increased in comparison: on average 1.5% in IR1 and 0.5% in IR5, reflecting increased detuning differences (see below). Also, the left-right symmetry in IR5 is broken in these corrections, favoring the left corrector (at 18%) over the right corrector (at 11%). Including the IR5 measurements in the correction (“MD6863 w/ IP5,” see Sec. III C), the IR5 symmetry is restored, yet the strength of the corrector right or IP1 is further increased, while the strength of the left corrector almost vanishes.

As none of the powering values are above 18% of the maximum powering of the magnets, we expect negligible impact on beam lifetime from the powering: they had to be powered to more than a quarter of their maximum strengths to show any measurable effect on lifetime (see [41]), which is discussed and confirmed in Sec. III G.

Figures 6 and 7 show the measured detuning change introduced by the crossing scheme during commissioning and MD, respectively. In blue the detuning change without correction is presented and in both measurements, the detuning from high-order errors can be observed. In contrast to what has been measured in 2018, were

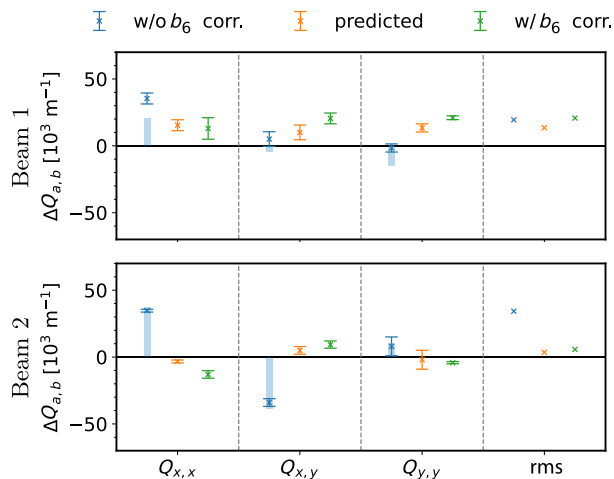


FIG. 6. Detuning differences as measured during commissioning 2022 between detuning with full crossing and at flat orbit for all detuning terms and the error-weighted root-mean-square (rms) over all terms. Measured values for the cross terms  $Q_{x,y}$  and  $Q_{y,x}$  have been averaged. Shown in blue is the measurement without dodecapole correction applied as circle with error bars and the detuning to be compensated by the correction as simulated via the bar. In orange the predicted detuning, estimated from measurement and the simulated correction value, is shown. The data in green are the actual measured detuning change with crossing angle after dodecapole correction.

mostly beam 1 had been affected, we now see in beam 1 big changes only in the direct horizontal term ( $Q_{x,x}$ ). In beam 2 on the other hand,  $Q_{x,x}$  and the cross term  $Q_{x,y}$  are majorly spoiled. The strongest feed-down was experienced in the cross term of beam 2 during MD, resulting in a change of detuning of more than  $50 \times 10^3 \text{ m}^{-1}$  in absolute value.

Blue vertical bars show the expected detuning change to be compensated by the correction, based on the simulation results. We see that for both corrections, the measured data could not be matched perfectly. The expected residual detuning differences after correction, calculated from measurement and simulated correction, are presented in orange. The figures show that  $Q_{x,y}$  and  $Q_{y,y}$  in beam 1 are expected to be slightly spoiled to achieve the partial correction of  $Q_{x,x}$  in beam 1 and very good correction of all terms in beam 2. In the last column of the figures, the error-weighted root-mean-square [rms, where the mean is calculated in accordance with Eq. (18)] of all terms is shown. This metric has been chosen to easily visualize the efficacy of the correction, as it reflects the optimization approach of Eq. (28), albeit per beam. A total rms for both beams is not shown, as, in contrast to the varied detuning changes in the individual terms, the validity of the corrections in this paper when presented per beam is clearly visible. From the rms, the net positive effect of the correction can be recognized immediately: Before correction, beam 2 shows a rms measured difference of  $34 \times 10^3 \text{ m}^{-1}$  (commissioning) and  $40 \times 10^3 \text{ m}^{-1}$  (MD6863) while the rms of beam 1 is much smaller at  $19 \times 10^3 \text{ m}^{-1}$  (commissioning)

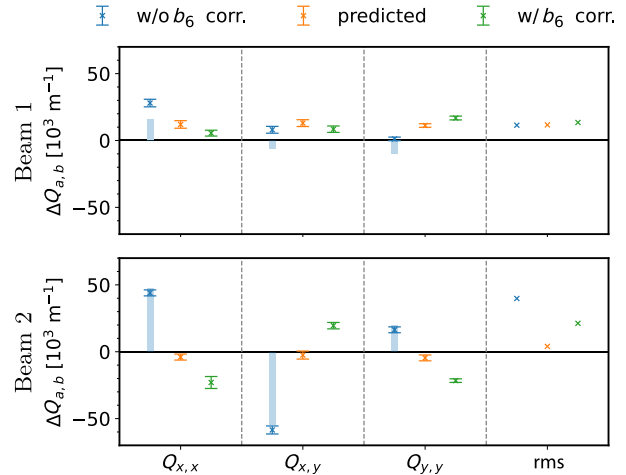


FIG. 7. Detuning differences during MD6863, presented in the same manner as the data in Fig. 6.

and  $11 \times 10^3 \text{ m}^{-1}$  (MD6863). In turn, beam 2 is expected to be very well corrected, while beam 1 will see a lesser improvement, if any.

In green the actual measured detuning difference still present in the machine after correction is shown. In general, we see that for both corrections, all terms have been “overcorrected.” This makes the rms for most measurements worse than expected, yet still resulting in an overall significant improvement: Beam 1 has been slightly spoiled by  $+1.3 \times 10^3 \text{ m}^{-1}$  (commissioning) and  $+2 \times 10^3 \text{ m}^{-1}$  (MD6863), while beam 2 has been drastically improved by  $-29 \times 10^3 \text{ m}^{-1}$  (commissioning) and  $-19 \times 10^3 \text{ m}^{-1}$  (MD6863).

The origin of this overcorrection could not yet be exclusively identified. Possible candidates are mismatches in orbit or  $\beta$  function between the model and the machine, uncertainties in the power supply of the correctors, as well as in Eq. (28) unaccounted second-order effects, e.g., due to feed-down to sextupole fields. Uncertainties on orbit and  $\beta$  function due to misalignments of the corrector magnets has been investigated in a simulation study: Pessimistically assuming the correctors to be misaligned with Gaussian distributions of  $\sigma = 1 \text{ mm}$  [88] and a Gaussian distributed  $\beta$  beating of  $\sigma = 5\%$ , the expected detuning can be calculated using the correction strengths “MD6863 w/ IP5” from Table III and Eq. (9). The resulting detuning distributions are shown in Fig. 8 and have a mean standard deviation, over terms and beams, of  $14 \times 10^3 \text{ m}^{-1}$ . Further simulations with the same parameters realizing only  $\beta$  beating show a mean  $\sigma$ , over terms and beams, of  $4 \times 10^3 \text{ m}^{-1}$  while simulations realizing only misalignments give a mean  $\sigma$  of  $13 \times 10^3 \text{ m}^{-1}$ , showing that including the measured  $\beta$  into calculations will not majorly improve the correction, as the uncertainty on alignments is the dominating factor. From these standard deviations we see, that the uncertainty we have from

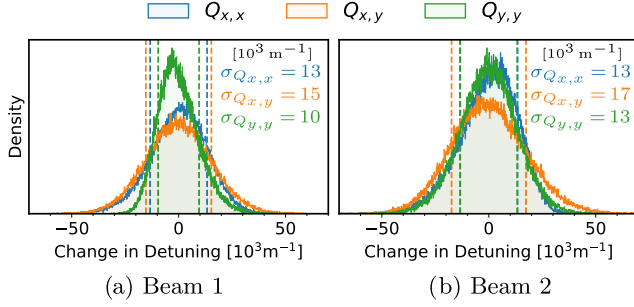


FIG. 8. Histograms of detuning changes for 100 000 realizations of random misalignments and random  $\beta$  beating at the corrector elements. Both parameters are taken from Gaussian distributions: The distribution parameters for the misalignments are  $\mu = 0$  mm,  $\sigma = 1$  mm and the for the  $\beta$ -ratio  $\mu = 1$ ,  $\sigma = 0.05$ . The random values are applied individually to the corrector magnets left and right of IP1 and IP5. From each realization, all three detuning terms were calculated from  $Q_{a,b} = \sum_w \frac{1}{2} (\Delta x_w^2 - \Delta y_w^2) \tilde{\beta}_{a,b;w} K_6 L_w$  using the correction “MD6863 w/ IP5” in Table III for the strengths of the corrector elements  $w$ . The dashed vertical lines are set at the standard deviation of the resulting detuning distribution and their values are shown.

possible misalignments of the corrector magnets is compatible with the difference we see between the predicted and measured values after correction in Figs. 6 and 7, meaning that there is a possibility that without better knowledge of the corrector (mis-)alignments we could be at the limit of the correction accuracy. This knowledge could be obtained in the future, e.g., by investigating the feed-down to tune from the nested sextupole correctors in the nonlinear corrector package [89].

In Sec. III C, we will discuss an enhancement of the corrections, by attempting to correct only the  $b_6$  contribution and correct the errors more locally by gaining information about the contribution per IP. This was done to gain a better understanding of the origin of the errors and also to improve the correction accuracy. Due to the limited availability of “beam-time” at the LHC for this study, the improvements from advanced corrections could not be extensively tested in the machine.

In general, despite the observed discrepancies between the expectation from simulation and measurement, both tested corrections are well able to reduce the common detuning introduced by high-order errors in the two beams, and partially even out the contribution per beam.

### C. Error sources

In addition, studies were carried out during MD to identify the sources of the errors, i.e., whether their origin lies in decapole or dodecapole order and if they stem from IR1 or IR5. To attain this objective, the crossing bump at IP1 was kept deactivated, while measurements were performed with nominal crossing angle in IP5 and also with opposite angle sign.

### 1. Multipole order

As there is only horizontal orbit in IP5 in our measurements (see Table I), we know from Eqs. (8) and (9) using the abbreviations Eqs. (11) and (12):

$$Q_{a,b}^\emptyset = \sum_w K_4 L_w \tilde{\beta}_{a,b;w}$$

$$Q_{a,b}^- = \sum_w \left( K_4 L_w - \Delta x_w K_5 L_w + \frac{1}{2} \Delta x_w^2 K_6 L_w \right) \tilde{\beta}_{a,b;w}$$

$$Q_{a,b}^+ = \sum_w \left( K_4 L_w + \Delta x_w K_5 L_w + \frac{1}{2} \Delta x_w^2 K_6 L_w \right) \tilde{\beta}_{a,b;w}, \quad (30)$$

distinguishing between the cases “ $\emptyset$ ” for flat orbit, “+” for positive nominal crossing angle at IP5 and “-” for negative angle. Here it is also assumed that each element  $w$  sees an equal-in-magnitude but opposite in sign horizontal orbit offset  $x_w$  when switching crossing angle sign. This symmetry is established in the model orbit, as shown in Fig. 9, and in good approximation present in the machine, due to the orbit feedback mentioned in Sec. II D, but future studies of the actual magnet misalignments in the IRs could again be beneficial to further improve upon the following considerations. The contributions to the detuning change in IR5

$$\Delta Q_{a,b}^{(\text{IP5}+160 \mu\text{rad})} = Q_{a,b}^+ - Q_{a,b}^\emptyset$$

$$= \sum_w \left( \Delta x_w K_5 L_w + \frac{1}{2} \Delta x_w^2 K_6 L_w \right) \tilde{\beta}_{a,b;w}, \quad (31)$$

from each multipole order can be calculated from the measured data using Eq. (30)

$$\Delta Q_{a,b}^{(\text{from } b_5)} = \sum_w \Delta x_w K_5 L_w \tilde{\beta}_{a,b;w} = \frac{1}{2} (Q_{a,b}^+ - Q_{a,b}^-) \quad (32a)$$

$$\Delta Q_{a,b}^{(\text{from } b_6)} = \sum_w \frac{1}{2} \Delta x_w^2 K_6 L_w \tilde{\beta}_{a,b;w}$$

$$= \frac{1}{2} (Q_{a,b}^+ + Q_{a,b}^- - 2Q_{a,b}^\emptyset). \quad (32b)$$

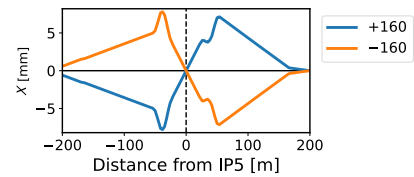


FIG. 9. Horizontal orbit of beam 1 in IR5 for crossing schemes with  $\pm 160 \mu\text{rad}$  half-angles, demonstrating the symmetry with respect to the  $x$  axis of the two scenarios.

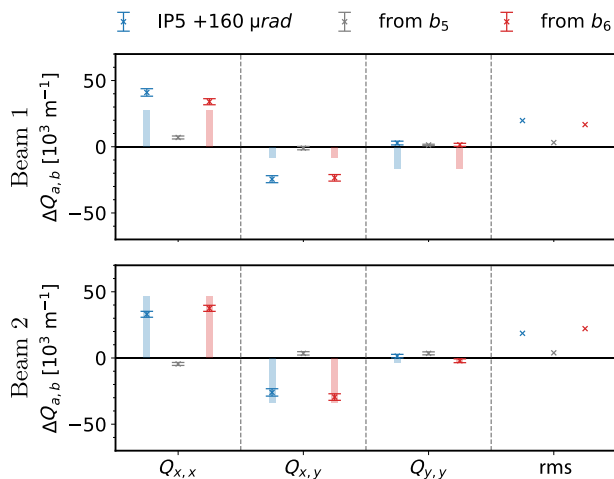


FIG. 10. Detuning changes between the scenario of positive crossing angle at IP5 and flat orbit as measured during MD. Shown are the contributions to the full detuning change (blue) from decapole sources (gray) and dodecapole sources (red) as calculated from Eq. (32), for all detuning terms individually and the error-weighted root-mean-square (rms) over all terms. Vertical bars show the detuning compensated by the correction “MD6863 w/o IP5” in Table III according to Eqs. (8) and (9). Measured values for the cross terms  $Q_{x,y}$  and  $Q_{y,x}$  have been averaged.

The results are presented in Fig. 10, which clearly shows that the main contribution to the detuning change in IR5 with positive crossing stems from dodecapole sources, while the contribution from decapoles is only around 14% in rms. This finding is in line with the expectation from magnetic measurements and simulations [25] as dodecapole fields are the first allowed harmonic of quadrupole magnets [36].

Another insight we achieve from Fig. 10 is that in beam 1, the contributions from  $b_5$  and  $b_6$  add up, whereas in beam 2, they partly cancel each other, leading to the higher detuning differences measured in beam 1 with positive IP5 crossing. We also see that the  $b_6$  corrections applied in IR5, calculated by Eqs. (8) and (9) and shown as green vertical bars, compensate for the  $b_6$  contribution in beam 2 very well, but in beam 1 only manage to do so for the horizontal term. This could be because no distinction was made between contributions from IR1 and IR5 when calculating the correction, which could be overcome by targeting also the IR5 measurement in Eq. (28); another reason could be, that  $\beta$  function and orbit at the corrector magnets are not representative for  $\beta$  and orbit at the actual sources, making it impossible to find a perfect match.

## 2. Interaction region

Figure 11 is showing again the change in detuning between full-crossing scheme and flat orbit as measured during MD before dodecapole corrections (blue), but this

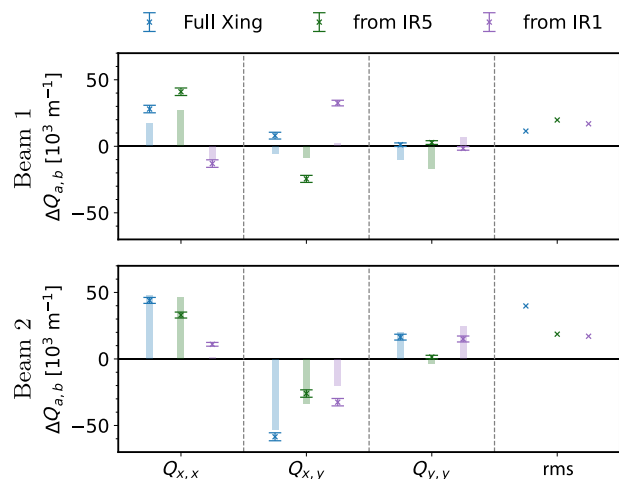


FIG. 11. Detuning changes as measured during MD without dodecapole correction between the detuning with full crossing and flat orbit (blue) as well as the scenario of positive crossing at IP5 (green), for all detuning terms individually and the error-weighted root-mean-square (rms) over all terms. For convenience, the detuning contribution from IR1 (purple) has been calculated from the difference of the two measurements. Vertical bars show the detuning compensated by the correction “MD6863 w/o IP5” in Table III according to Eqs. (8) and (9).

time split into contributions from the IR5 (green) and IR1 (purple), where the former comes from the measurement with positive crossing angle at IP5 and the latter is calculated from the difference between the full crossing scheme and the IR5 measurements. The plots show that contributions from IR1 change sign between beams, whereas in IR5, the sign of the detuning difference stays the same. This leads to the IR contributions adding up in beam 2 and canceling each other partly in beam 1, the opposite effect as discovered between  $b_5$  and  $b_6$  contributions in IR5. The effect from different orders is shadowed by the effect from different IRs, leading to the higher measured detuning difference with the full crossing scheme in beam 2.

While the horizontal term shows a much larger contribution from IR5, the other terms are similar in absolute contribution from both IRs, leading to fairly equal rms contributions from both IRs. This is in contrast to the behavior observed in 2018, where the main contribution had come from IR5; see Table II and [31]. The expected detuning to be compensated by the corrections, as calculated by Eqs. (8) and (9), is presented again through the vertical bars in Fig. 11: in total (blue) and split into the contributions per IR (green and purple). The correction seems to be good locally in only half of the terms, that is, in the horizontal direct term of beam 1 and in the cross terms of beam 2 as well as beam 2’s vertical direct term. Despite stronger powering of the IR5 correctors, overcorrection of IR5 and undercorrection of IR1 is only visible in beam 2’s  $Q_{x,x}$  and  $Q_{x,y}$ , signifying that the difference in powering is an effect of the different orbit and  $\beta$  functions at the

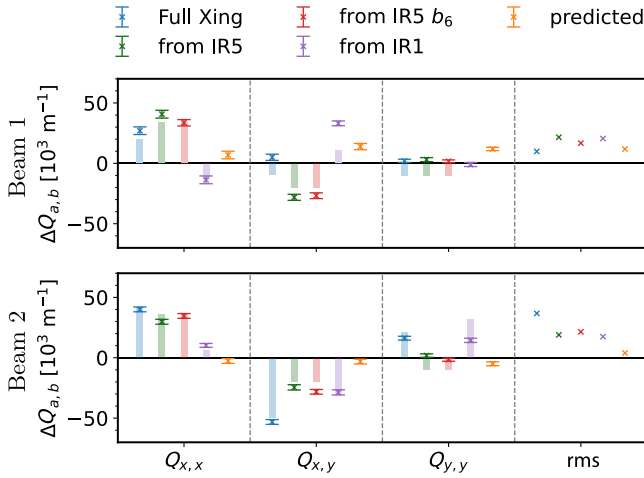


FIG. 12. Detuning changes as measured during MD without dodecapole correction between the detuning with full crossing and flat orbit in blue, as well as the measured individual contributions from the IR5 dodecapole fields in red, and the total contributions from IR5 (green) and IR1 (purple), as well as the predicted value after correction in orange. The data are presented for all detuning terms and the error-weighted root-mean-square (rms) over all terms. Measured values for the cross terms  $Q_{x,y}$  and  $Q_{y,x}$  have been averaged.

correctors of the IRs and not of different error distributions between the IRs.

### 3. Improved corrections

Additional context about the locality and field order can be supplied to improve upon the corrections as discussed so far. This information, gained through the measurement of activating the crossing bump at the IPs individually, as well as with opposite sign, can be incorporated either through boundary restrictions on the linear equation system, as had been attempted in [79], or by including the measurements as additional targets into Eq. (28). The latter has been tested in simulations, and the results, presented in Fig. 12, are very promising: Despite the additional restrictions on the correction, the estimated rms does not change compared to the “global” correction. On the other hand, in all terms, the correction is able to target  $b_6$  in IP5 and the contribution per IP more closely than the previous correction, increasing locality of the correction.

These corrections have since been incorporated operationally into the LHC, replacing the commissioning corrections which were used from June 4, 2022 to October 2, 2022. Yet, due to the LHC running now for luminosity production, they could not be investigated in detail by amplitude detuning measurements.

### D. Second-order detuning

Up until now, corrections were calculated based on the assumption that the second-order terms in amplitude in

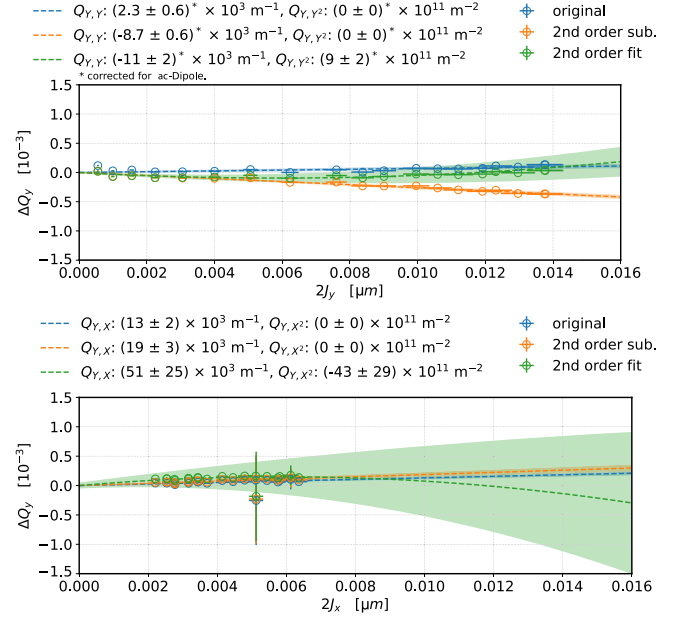


FIG. 13. Data of the measured vertical detuning in beam 2 without dodecapole correction at flat orbit from MD. The data points of the detuning measurement are presented as in Figs. 3 and 5. On top of these, the linear polynomial fits on original measured data (blue) and the measured data after subtraction of the second-order contribution as calculated from the “MD6863 w/ IP5” corrections in Table III (orange) are shown. In green, the original data are shown again, but here a second-order polynomial fit is performed. Dashed lines show the polynomial fit to the data points, while the colored area covers one standard deviation of the fit. The constant part has been subtracted from the fit and its respective data points.

Eq. (7) are negligible and the main contribution to detuning from dodecapoles comes from feed-down to first-order detuning. Assuming the dodecapole fields from the correctors to be representative for the IR, just with opposite sign, the “MD6863 w/ IP5” correction calculated in the previous chapter and Eq. (10) could be used to calculate their contributions to second-order detuning. It was found that for large kicks, that is at 0.02 mm, the contributions could be up to 50% of the total measured detuning.

To determine the influence of the second-order detuning on the first-order fits, two approaches have been tested: In the first approach, the measurement data have been fit with a second-order polynomial, still using ODR to include the measurement uncertainties. The second-order coefficients could in principle then also be used to extend the equation system [Eq. (28)], adding new rows for the  $\Delta Q_{a,b,c}^{(BN)}$  on the left-hand side, and new matrix elements from Eq. (10)

$$M_{a,b,c;w}^{(BN)} = \tilde{\beta}_{a,b,c;w}^{(BN)} \quad (33)$$

on the right-hand side. As, for example, shown in Fig. 13, second-order polynomial fitting lead only to reasonable

TABLE IV. Summary of amplitude detuning measurements after subtracting second-order contributions calculated from the “MD6863 w/ IP5” corrections (Table III) following the conventions in Table II. In parenthesis, the difference ( $\Delta$ ) to the original detuning values is given.

	$Q_{x,x}$ ( $10^3\text{m}^{-1}$ )	( $\Delta$ )	$Q_{y,x}$ ( $10^3\text{m}^{-1}$ )	( $\Delta$ )	$Q_{x,y}$ ( $10^3\text{m}^{-1}$ )	( $\Delta$ )	$Q_{y,y}$ ( $10^3\text{m}^{-1}$ )	( $\Delta$ )
2022 MD6863 w/o $b_6$	$-22 \pm 2$	(-4)	$37 \pm 2$	(+5)	$27 \pm 4$	(+4)	$-7.7 \pm 0.7$	(-7.7)
Flat orbit	$-27.1 \pm 1.8$	(-8)	$19 \pm 3$	(+6)	$23.9 \pm 2.0$	(+12)	$-13.1 \pm 0.8$	(-16.5)
2022 MD6863 w/o $b_6$	$6 \pm 2$	(-4)	$42.2 \pm 2.0$	(+5)	$30 \pm 2$	(+3)	$-4.1 \pm 1.0$	(-6.1)
IP1 & 5@ $\mp 160 \mu\text{rad}$	$17.5 \pm 1.3$	(-3.4)	$-43 \pm 3$	(-4)	$-31 \pm 3$	(+12)	$4.8 \pm 0.8$	(-14.9)
2022 MD6863 w/o $b_6$	$16 \pm 2$	(-7)	$9 \pm 3$	(+7)	$0.3 \pm 1.4$	(+4.0)	$-6.2 \pm 1.1$	(-9.2)
IP5@ + 160 $\mu\text{rad}$	$5.8 \pm 1.2$	(-4.8)	$-4 \pm 3$	(+5)	$-6.5 \pm 1.9$	(+9)	$-7.7 \pm 0.6$	(-13.0)
2022 MD6863 w/o $b_6$	$3.0 \pm 1.0$	(-5.9)	$8 \pm 4$	(+5)	$3.2 \pm 0.5$	(+4.1)	$-9.0 \pm 0.4$	(-9.2)
IP5@ - 160 $\mu\text{rad}$	$15.2 \pm 1.8$	(-5)	$-11 \pm 3$	(+4)	$-12.4 \pm 1.4$	(+10.9)	$-16.4 \pm 1.8$	(-15)

results where high kick amplitudes could be reached (Fig. 13, top), yet lead to an overfitting on measurements where their maximum amplitude was below 0.01 mm and, in conclusion, to unreasonable and unusable results for most measurements (Fig. 13, bottom). This approach has hence been discarded for the data at hand but could be usable in future measurements if consistent large amplitude excitations can be achieved.

In the second approach, the values of the “MD6863 w/ IP5” corrections (Table III) at the correctors were used to calculate the tune shift from second order in amplitude at each conducted kick. These contributions have then been subtracted from the measured data, neglecting the error bars on the corrections, but accounting for any coefficients due to the forced oscillations [33]. Subsequently, first-order polynomial fits were applied to the resulting data (e.g., shown in Fig. 13). The found detuning coefficients are given in Table IV, which also provides the differences to the original data in Table III. Despite the changes in detuning coefficients, the corrections, evaluated from these and given in Table V, are still within 10% of the originally calculated corrections, apart from the corrector left of IP1 which almost doubled in strength but is still lower than a fifth of the powering of the other correctors.

Interestingly, the correction strengths have overall been increased by this second approach, hinting at a compensation between first- and second-order terms. This approach could be extended to an iteration scheme, in the hopes that the corrector values will converge toward an optimal value.

Due to time constraints and because the correction has not dramatically changed after this first iteration, this fine tuning has not been conducted. In fact, as most corrector values are within error bars of each other (apart from the left corrector in IP5), it is doubtful that any difference would be perceptible given the accuracy of the measurements.

### E. Comparison with the magnetic model

Magnets in the LHC have undergone magnetic measurements before installation, the results of which have been collected in the “Field Model of the LHC” (FiDeL [90]) which is the basis for the so-called “Windows Interface to Simulation Errors” (WISE [91]). The errors on the field measurements lead to 100 different realizations, or “seeds,” of the errors and are used to simulate realistic error scenarios in the LHC [92] and HL-LHC.

In the past, differences had been found between corrections obtained from simulation and beam-based methods [93]. To test the agreement for the dodecapole corrections, a basic simulation has been set up, following the description in Sec. II G, but including dodecapole errors from the WISE tables. Previous studies have shown that, as the  $\beta$  function for squeezed optics varies dramatically in the IR, the MQXA magnets of the triplets [4] should be split into hard-edge bodies and heads [21,94,95]. This procedure is applied to the simulation at hand. Errors are then corrected by minimizing the contribution to first order amplitude via feed-down locally in IR1 and IR5 as well as to the global detuning. This is achieved by optimizing an equation system

TABLE V. Dodecapole-corrector strength values ( $K_6$ ). In parenthesis, the percentage of the maximum powering at 6.8 TeV is given. Shown are again the values for the *Improved Corrections* of “MD6863 w/ IP5” as in Table III as well as the corrector strengths calculated in the same manner from the detuning values of Table IV, with the second-order contributions subtracted.

	IP1		IP5	
	MCTX.3L1 ( $10^3\text{m}^{-6}$ )	MCTX.3R1 ( $10^3\text{m}^{-6}$ )	MCTX.3L5 ( $10^3\text{m}^{-6}$ )	MCTX.3R5 ( $10^3\text{m}^{-6}$ )
Original values	$0.493 \pm 192$ (1%)	$-3.982 \pm 188$ (11%)	$5.003 \pm 132$ (14%)	$-5.032 \pm 162$ (14%)
Second-order subtracted	$0.816 \pm 197$ (2%)	$-4.232 \pm 202$ (12%)	$5.363 \pm 142$ (15%)	$-5.011 \pm 167$ (14%)

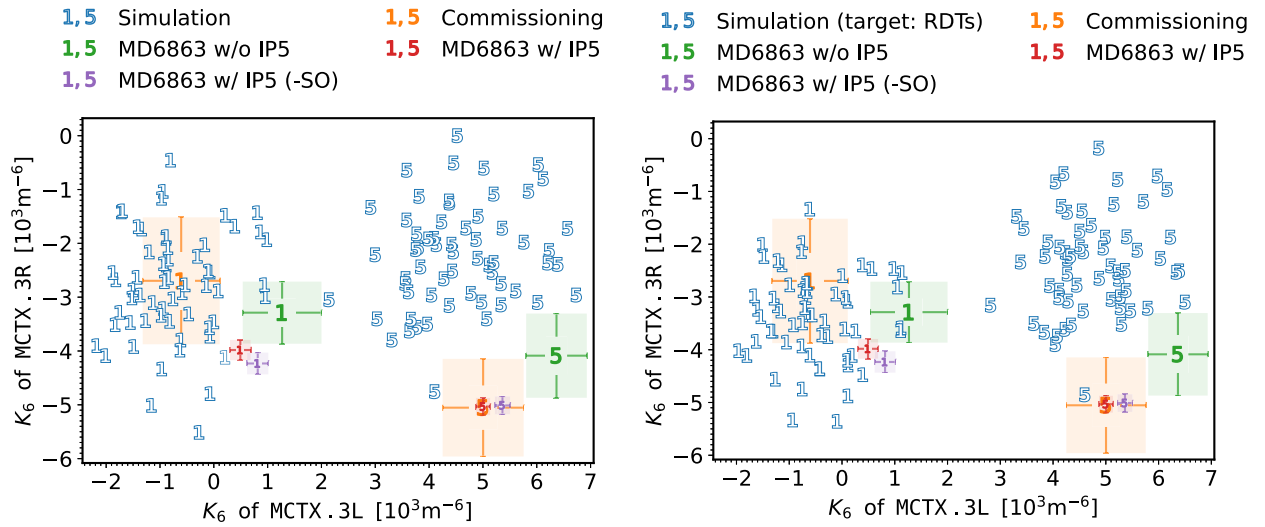


FIG. 14. Comparison of dodecapole corrections from simulations based on the magnetic model (blue), with the corrections calculated from the beam-based measurements of feed-down to amplitude detuning. The plot shows the strength of the dodecapole field ( $K_6$ ) of the right dodecapole corrector (MCTX . 3R [15]) over the strength of the left dodecapole corrector (MCTX . 3L [15]). The markers express the IR of the correctors: “1” for IR1 and “5” for IR5. In the simulation  $b_6$  errors are assigned from 100 different WISE-seeds and corrected by minimizing feed-down to first-order amplitude detuning locally in the IRs as well as globally (left) or locally correcting the dodecapole RDT  $f_{6000}$  (right). The values of the beam-based corrections correspond to the calculated powering of Tables III and V, where “(-SO)” refers to the values with second-order detuning subtracted. Their uncertainties are represented by the reach of the errorbars and the respective surrounding area of the same color.

as in Eq. (28), yet with  $\Delta Q_{a,b}$  not from measurements but from the feed-down to first-order detuning from the errors. For comparison, the dodecapole errors are also targeted by locally minimizing the dodecapole RDTs in the IRs using the correction algorithm [96] presented in [97,98]. The latter is our standard way to calculate corrections in simulations based on magnetic models, yet here the correction target is inherently different to the beam-based measurements.

Figure 14 shows both correction approaches in two plots: on the left, the results from targeting feed-down to first-order detuning is shown, on the right, the RDT-based corrections are presented. The corrector strengths from the simulations are in blue and are compared to the three different beam-based corrections as in Table III: from commissioning (orange), from MD without the IR5 measurements (green) and from the *Improved corrections* including IR5 measurements (“MD6863 w/ IP5” in Table III, red). For completeness also the in Sec. III D explored correction values after subtracting the second-order contributions are shown (purple). In both plots, the beam-based corrections in IR1 align closely with the outcomes of the various seeds, in the right corrector of IR5, only very few seeds predict that large correction strengths. In the case of targeting the feed-down to detuning, none of the seeds agree for both correctors of IR5 at the same time. However, a few of the seeds on the periphery of the simulation results are close to the beam-based results, and there is always a seed lying within the errorbar of an individual corrector strength of any beam-based correction.

From the comparison between the two different simulation targets, we see that depending on which observable is considered, i.e., either feed-down to detuning or RDTs, the optimal corrector powering can be different, only partially correcting the respective other observable.

We find, therefore, beam-based and magnetic measurements in agreement, within error bars of each other, increasing the confidence in the beam-based dodecapole corrections as well as the magnetic model, which is regularly (e.g., [25,38,79,99–101]) used to represent the LHC and HL-LHC in simulations.

### F. Influence on Landau damping

Given the  $\beta^* = 30$  cm optics investigated, the introduced detuning from the Landau octupoles at their nominal strength of 433 A [102] is about  $Q_{x,x} = Q_{y,y} = 177 \times 10^3 \text{ m}^{-1}$  in the direct terms and  $Q_{x,y} = -100 \times 10^3 \text{ m}^{-1}$  in the cross term. As mentioned in Sec. II G, in this study, we are not trying to “support” the Landau damping by matching the detuning to these values but to optimize machine control by reducing the detuning from errors in favor of an improved estimate on the residual detuning regardless of applied crossing scheme.

The two detuning terms showing the highest achieved correction of unwanted detuning, with regard to the change in absolute detuning between flat optics and with crossing angles, from the original correction applied during the MD (Fig. 7), are the cross term of beam 2, which was improved



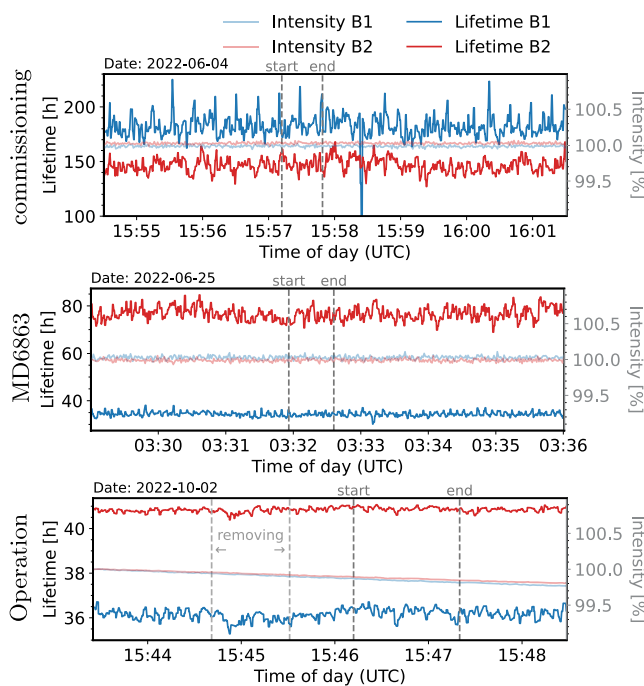


FIG. 15. Beam lifetime (from BLMs) and intensity (from BCTFR, normalized to the first datapoint) before and after the trim of the  $b_6$  corrections during commissioning 2022 (top), MD (middle). The bottom plot shows the application of the “MD6863 w/ IP5” corrections (Table III), during operation, after trimming out (“removing”) the previously incorporated dodecapole correction from commissioning. Start and end of the trimming processes are marked in the plot.

by an equivalent of 33% in MO powering, and the direct horizontal term in beam 1, which improved by an equivalent of 12%. For the improved corrections (Fig. 12), the terms with the highest improvements in the same metric are the cross term and direct horizontal term of beam 2, with respective predicted improvements of 53% and 16% of MO-induced detuning.

In conclusion, the dodecapole corrections allow for a substantial increase in the control of the introduced Landau damping from the MOs in the machine, independent of the actual damping scheme.

### G. Beam lifetime

During the trims of the dodecapole corrections into the machine, beam lifetime has been extracted from the beam loss monitors (BLMs) and beam intensity from the fast beam current transformer (BCTFR) and are shown in Fig. 15.

There is no obvious change on these parameters detectable after powering the dodecapole corrections, neither during commissioning (top plot) nor during MD (middle plot), when only noncolliding pilot bunches were circulating in the LHC. During operation, i.e., with colliding beams and a full filling scheme, trimming out the commissioning corrections and trimming in the *Improved corrections*

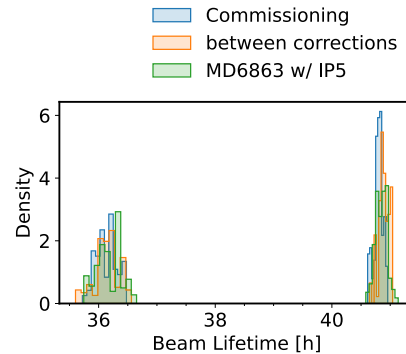


FIG. 16. Beam lifetime as histograms of the BLM data of 41 s intervals before trimming out the commissioning correction (blue), between corrections (orange), and after trimming in the improved correction, including all measurements from MD. The left cluster shows data from beam 1 while the right cluster shows beam 2 data. The same data over time can be seen in the bottom plot of Fig. 15.

including IR5 measurements, the lifetime drops slightly during the trims and recovers thereafter, as seen in the bottom plot of Fig. 15. The histograms in Fig. 16 show that the mean beam lifetime in 41 s before trimming out the old corrections, between the two corrections and after trimming in the new corrections is preserved. This behavior is expected in the LHC, where any change in parameters can lead to a temporary change in expected beam lifetime. There is no additional loss of beam intensity, apart from the visible burn-off due to collisions.

These measurements are in line with the measurements performed during MD3312 [41] and the studies performed in [25], in which the dodecapole correctors were powered to higher values before an impact on beam lifetime became visible.

## IV. CONCLUSION AND OUTLOOK

### A. Summary

In this paper, the results of the amplitude detuning measurements conducted during the LHC commissioning for Run 3 in 2022 and during a dedicated machine development session, have been presented, which were performed to identify and correct detuning originating in the feed-down from high-order nonlinear errors in the IRs. Dodecapole corrections were calculated, and for the first time integrated into the LHC operation, effectively reducing the rms of the detuning change over all terms and both beams, therefore allowing, e.g., for tighter control of Landau damping. Corrections calculated via this beam-based method agree very well with corrections calculated in simulations using the magnetic model. Incorporation of the corrections did not spoil beam lifetime in the LHC.

### B. Conclusions and outlook

We have shown that with the measurement method at hand, sources of the detuning could be identified: In IR5, a

clear origin from dodecapole errors has been seen and it could also be concluded that both IRs contribute equally to the observed detuning. To advance the corrections in the future, one could even further improve on the locality of the correction by targeting only the dodecapole contributions in both IRs specifically. To accomplish this, one more measurement with opposite-sign crossing angles is needed, either with crossing bumps around IP1 only or opposite-sign full crossing in both IRs.

As the presented results show, magnetic field errors up to dodecapole order can be identified using feed-down to amplitude detuning as observable. This can be achieved with our current measurement methods. For HL-LHC, these results are vital, as the influence of high-order nonlinearities is foreseen to be increased. Not only confirms our study the expectations of [25] but also establishes that the therein described effort for high-order field error measurements can be reduced: If the quality of the measurements is good, i.e., there is a low error bar on the data points, calculating the dodecapole contribution from only three data points yields reliable results and can lessen the workload estimated in [25]. In case of larger error bars, measurements at additional working points might be necessary to establish a statistically meaningful fit. Distinction between the different orders will become of more importance with the HL-LHC upgrade, as they can be targeted individually by the improved nonlinear corrector package, containing correctors for all normal and skew fields up to dodecapole order. In this advanced machine configuration, it is also foreseen that the impact from the high-order field errors will be more significant, due to the increased optics sensitivity in the IRs [38] and high-order corrections will be needed to allow prolonged machine operation [25].

We have seen from simulations, that misalignment of the corrector magnets is a possible candidate for the observed overcorrection. Better knowledge of these misalignments, e.g., gained from dedicated feed-down studies [89], could help to further improve the accuracy of the correction.

Of further interest in the LHC is also the study of the change in free and forced dynamic aperture upon applying the dodecapole corrections [67,103].

## ACKNOWLEDGMENTS

The authors' copious thanks go to the CERN Operations Group and LHC Operators and Engineers in Charge, for the significant amount of support lent during commissioning and machine development sessions, especially T. Argyropoulos, M. Hostettler, and G. Trad who were managing the LHC during the measurements presented. Similarly, deep thanks go to the LHC Collimation team and CERN Beam Instrumentation Group, without their work, amplitude detuning studies in the LHC would not have been possible. The authors want to also show their deep gratitude to B. Dalena for the discussion of the simulation results and for sharing data from their own studies about the

ITs, P. Hagen for making the WISE errortables available to us, as well as M. Giovannozzi for his help navigating different LHC errortables. As always, great thanks go the LHC Optics Measurement and Correction team for their broad assistance during commissioning and in general all support given throughout the years. A heartfelt thanks also goes out to M. Hofer, for keeping his door open to any questions and for his help with the bibliography. J. Dilly would also like to thank Professor Dr. A. Jankowiak for his wonderful Ph.D. co-supervision and insightful comments. This work has been supported by the HiLumi Project and has been sponsored by the Wolfgang Gentner Program of the German Federal Ministry of Education and Research.

- 
- [1] E. H. Maclean, 4.2.2 Amplitude detuning, in *Modelling and Correction of the Non-Linear Transverse Dynamics of the LHC from Beam-Based Measurements* (Herford College, University of Oxford, 2014).
  - [2] E. H. Maclean, R. Tomás, F. S. Carlier, M. S. Camillocci, J. W. Dilly, J. Coello de Portugal, E. Fol, K. Fuchsberger, A. Garcia-Tabares Valdívieso, M. Giovannozzi, M. Hofer, L. Malina, T. H. B. Persson, P. K. Skowronski, and A. Wegscheider, New approach to LHC optics commissioning for the nonlinear era, *Phys. Rev. Accel. Beams* **22**, 061004 (2019).
  - [3] J. Gareyte, J. P. Koutchouk, and F. Ruggiero, Landau damping, dynamic aperture and octupoles in LHC, CERN, LHC Project Report No. LHC-Project-Report-91, 1997.
  - [4] O. S. Brüning, J. Poole, P. Collier, P. Lebrun, R. Ostojic, S. Myers, and P. Proudlock, LHC design report, LHC Project CERN Report No. CERN-2004-003-V-1, 2004, <https://dx.doi.org/10.5170/CERN-2004-003-V-1>.
  - [5] A. Bazzani, G. Servizi, E. Todesco, and G. Turchetti, A normal form approach to the theory of nonlinear betatron motion, CERN, Geneva, Report No. CERN-94-02, 1994, <https://dx.doi.org/10.5170/CERN-1994-002>.
  - [6] E. H. Maclean, R. Tomás, M. Giovannozzi, and T. H. B. Persson, First measurement and correction of nonlinear errors in the experimental insertions of the CERN Large Hadron Collider, *Phys. Rev. ST Accel. Beams* **18**, 121002 (2015).
  - [7] E. H. Maclean, F. Carlier, J. M. Coello de Portugal, A. Garcia-Tabares, M. Giovannozzi, L. Malina, T. Persson, P. Skowroński, and R. Tomás, New methods for measurement of nonlinear errors in LHC experimental IRs and their application in the HL-LHC, in *Proceedings of IPAC2017, Copenhagen, Denmark* (JACoW, Geneva, Switzerland, 2017), <https://dx.doi.org/10.18429/JACoW-IPAC2017-WEPIK093>.
  - [8] J. Wei, W. Fischer, V. Ptitsyn, R. Ostojic, and J. Strait, Interaction region local correction for the Large Hadron Collider, in *Proceedings of the 18th Particle Accelerator Conference, New York, 1999* (IEEE, New York, NY, 1999), <https://dx.doi.org/10.1109/PAC.1999.792983>.
  - [9] J.-P. Koutchouk, F. Pilat, and V. Ptitsyn, Beam based measurements of field multipoles in the RHIC low

- beta insertions and extrapolation of the method to the LHC, in *Proceedings of 2001 Particle Accelerator Conference, Chicago, IL* (IEEE, New York, 2001), Vol. 3, pp. 1684–1686, <https://dx.doi.org/10.1109/PAC.2001.987148>.
- [10] O. S. Brüning, S. D. Fartoukh, A. M. Lombardi, F. Schmidt, T. Risselada, and A. Giovannozzi, Field quality issues for LHC magnets: Analysis and perspectives for quadrupoles and separation dipoles, in *Proceedings of 1st LHC Project Workshop, Chamonix, France* (CERN, Geneva, Switzerland, 2004).
- [11] R. Tomás, M. Giovannozzi, and R. de Maria, Nonlinear correction schemes for the phase 1 LHC insertion region upgrade and dynamic aperture studies, *Phys. Rev. ST Accel. Beams* **12**, 011002 (2009).
- [12] L. C. Teng, Error analysis for the low beta quadrupoles of the tevatron collider/location and strengths of correction dipoles in the low beta insertion, Fermilab Technical Report No. FERMILAB-TM-1097, 1982.
- [13] Y. Luo, M. Bai, J. Beebe-Wang, J. Bengtsson, R. Calaga, W. Fischer, A. K. Jain, N. Malitsky, S. Peggs, F. C. Pilat, V. Ptitsyn, G. Robert-Demolaize, T. Satogata, and S. Tepikian, Overview of magnetic nonlinear beam dynamics in RHIC, in *Proceedings of the 23rd Particle Accelerator Conference, Vancouver, Canada, 2009* (IEEE, Piscataway, NJ, 2009), WE6PFP006.
- [14] H. Sugimoto, *SuperKEKB*, Advanced Optics Control (CERN, Geneva, Switzerland, 2015).
- [15] M. Benedikt, J. Wenninger, D. Schulte, and F. Zimmermann, Challenges for highest energy circular colliders, Accelerators & Technology Sector Note CERN-ACC-2014-0153, 2014, <https://dx.doi.org/10.18429/JACoW-IPAC2014-MOXAA01>.
- [16] D. Schulte, *Optics Challenges for Future Hadron Colliders*, Advanced Optics Control, (CERN, Geneva, Switzerland, 2015).
- [17] E. Cruz Alaniz, R. Martin, E. H. Maclean, R. Tomas Garcia, and A. Seryi, Non linear field correction effects on the dynamic aperture of the FCC-hh, in *Proceedings of 8th International Particle Accelerator Conference, IPAC17, Copenhagen, Denmark* (JACoW, Geneva, Switzerland, 2017), TUPVA038, <https://dx.doi.org/10.18429/JACoW-IPAC2017-TUPVA038>.
- [18] O. Aberle *et al.*, High-luminosity Large Hadron Collider (HL-LHC): Technical Design Report, CERN Yellow Reports: Monographs, CERN, Geneva, Report No. CERN-2020-010, 2020, <https://dx.doi.org/10.23731/CYRM-2020-0010>.
- [19] G. Arduini, R. Bruce, R. D. Maria, M. Giovannozzi, G. Iadarola, J. Jowett, E. Métral, Y. Papaphilippou, and R. T. Garcia, Chapter 2: Machine layout and performance, in *High-Luminosity Large Hadron Collider (HL-LHC): Technical Design Report* (CERN, Geneva, Switzerland, 2020), Vol. 10, pp. 17–17, <https://dx.doi.org/10.23731/CYRM-2020-0010.17>.
- [20] F. S. Carlier, E. H. Maclean, L. E. Medina Medrano, L. Malina, D. Gamba, P. K. Skowronski, E. Fol, A. Wegscheider, A. Garcia-Tabares Valdivieso, and M. Giovannozzi, Optics Measurements and Correction Challenges for the HL-LHC, Accelerators & Technology Sector Note CERN-ACC-2017-0088, 2017.
- [21] X. Buffat, F. Carlier, J. Coello De Portugal, R. De Maria, J. Dilly, E. Fol, N. Fuster Martinez, D. Gamba, Garcia-Tabares Valdivieso, Ana, H. Garcia-Morales, M. Giovannozzi, M. Hofer, N. Karastathis, J. Keintzel, E. H. Maclean, L. Malina, T. H. B. Persson, P. K. Skowronski, F. Soubelet, R. Tomás, F. Van Der Veken, L. van Riesen-Haupt, A. Wegscheider, D. W. Wolf, J. F. Cardona, B. Dalena, and T. Pognat, Optics measurement and correction strategies for HL-LHC, CERN Accelerators & Technology Sector Note CERN-ACC-2022-0004, 2022.
- [22] E. H. Maclean, R. Tomás, F. Schmidt, and T. H. B. Persson, Measurement of nonlinear observables in the Large Hadron Collider using kicked beams, *Phys. Rev. ST Accel. Beams* **17**, 081002 (2014).
- [23] E. H. Maclean, R. Tomás, F. S. Carlier, J. Coello de Portugal, E. Fol, K. Fuchsberger, A. Garcia-Tabares Valdivieso, M. Giovannozzi, M. Hofer, L. Malina, T. H. B. Persson, P. K. Skowronski, M. Solfaroli Camillocci, and A. Wegscheider, Detailed review of the LHC optics commissioning for the nonlinear era, Accelerators & Technology Sector Note CERN-ACC-2019-0029, 2019.
- [24] F. S. Carlier, A nonlinear future: Measurements and corrections of nonlinear beam dynamics using forced Transverse Oscillations, Ph.D. thesis, Universiteit van Amsterdam, 2020, ISBN 9789464022148.
- [25] E. H. Maclean, F. S. Carlier, J. Dilly, M. Le Garrec, M. Giovannozzi, and R. Tomás, Prospects for beam-based study of dodecapole nonlinearities in the CERN High-Luminosity Large Hadron Collider, *Eur. Phys. J. Plus* **137**, 1249 (2022).
- [26] M. Gasior and R. Jones, High sensitivity tune measurement by direct diode detection, in *Proceedings of 7th European Workshop on Beam Diagnostics and Instrumentation for Particle Accelerators, DIPAC'05, Lyon, France* (CERN, Geneva, Switzerland, 2005), pp. 310–312.
- [27] A. Boccardi, M. Gasior, O. Jones, and R. J. Steinhagen, An overview of the LHC transverse diagnostics systems, LHC Project Report No. LHC-PROJECT-REPORT-1166, 2009.
- [28] A. Boccardi, M. Gasior, R. Jones, P. Karlsson, and R. J. Steinhagen, First results from the LHC BBQ tune and chromaticity systems, CERN, Geneva, Switzerland, Report No. LHC-Performance-Note-007, 2009.
- [29] E. H. Maclean, LHC Optics Commissioning in 2018, in *Proceedings of LMC Meeting* (CERN, Geneva, Switzerland, 2018).
- [30] E. H. Maclean, Nonlinear Optics MDs in 2018, *ABP-HSS Section Meeting* (CERN, Geneva, Switzerland, 2018).
- [31] J. Dilly, M. Albert, T. Argyropoulos, F. Carlier, M. Hofer, L. Malina, M. S. Camillocci, and R. Tomas, Report and analysis from LHC MD 3311: Amplitude detuning at end-of-squeeze, Accelerators & Technology Sector Note CERN-ACC-NOTE-2019-0042, 2019.

- [32] F. Pilat, Y. Luo, N. Malitsky, and V. Ptitsyn, Beam-based non-linear optics corrections in colliders, in *Proceedings of the 21st Particle Accelerator Conference, Knoxville, TN, 2005* (IEEE, Piscataway, NJ, 2005), pp. 601–605, <https://dx.doi.org/10.1109/PAC.2005.1590503>.
- [33] S. White, E. H. Maclean, and R. Tomás, Direct amplitude detuning measurement with ac dipole, *Phys. Rev. ST Accel. Beams* **16**, 071002 (2013).
- [34] E. H. Maclean, X. Buffat, F. Carlier, E. Fol, P. K. Skowronski, A. Garcia-Tabares Valdivieso, A. Wegscheider, T. H. B. Persson, R. Tomás, L. Malina, and J. Coello de Portugal, Nonlinear optics commissioning in the LHC, in *Proceedings of 7th Evian Workshop* (Evian Les Bains, France, 2016).
- [35] E. H. Maclean, R. Tomás, F. Carlier, M. Solfaroli Camillocci, J. Coello De Portugal, E. Fol, K. Fuchsberger, A. Garcia-Tabares Valdivieso, M. Giovannozzi, M. Hofer, L. Malina, T. H. B. Persson, P. K. Skowronski, and A. Wegscheider, New LHC optics correction approaches in 2017 (2017).
- [36] A. K. Jain, Basic theory of magnets, in *Proceedings of CERN Accel. Sch. Meas. Alignment Accel. Detect. Magn.* (CERN, Anacapri, Italy, 1997), pp. 1–26, <https://dx.doi.org/10.5170/CERN-1998-005.1>.
- [37] J. Dilly, E. H. Maclean, and R. Tomás, Corrections of feed-down of non-linear field errors in LHC and HL-LHC insertion regions, in *Proceedings of 12th International Particle Accelerator Conference, IPAC21, Campinas, Brazil* (JACoW, Geneva, Switzerland, 2021), MOPAB259, <https://dx.doi.org/10.18429/JACoW-IPAC2021-MOPAB259>.
- [38] J. Dilly, M. Giovannozzi, R. Tomás, and F. Van Der Veken, Corrections of systematic normal decapole field errors in the HL-LHC separation/recombination dipoles, in *Proceedings of 13th International Particle Accelerator Conference, IPAC22, Bangkok, Thailand* (JACoW, Geneva, Switzerland, 2022), WEPOPT059, <https://dx.doi.org/10.18429/JACoW-IPAC2022-WEPOPT059>.
- [39] E. H. Maclean, A. Wegscheider, M. Hofer, L. Malina, B. Dalena, P. K. Skowronski, E. Fol, F. S. Carlier, A. Garcia-Tabares Valdivieso, M. Giovannozzi, J. Coello de Portugal, R. Tomás, J. Dilly, E. Cruz Alaniz, and M. Solfaroli Camillocci, Report from LHC MD 2158: IR-nonlinear Studies, Accelerators & Technology Sector Note CERN-ACC-2018-0021, 2018.
- [40] E. H. Maclean, Prospect for High-Order Optics Measurement in the High-Luminosity LHC, in *Proceedings of ABP Information Meeting* (CERN, Geneva, Switzerland, 2020).
- [41] J. Dilly, M. Albert, F. Carlier, M. Hofer, L. Malina, M. Solfaroli Camillocci, R. Tomas, J. Coello De Portugal, B. Dalena, E. Fol, E. H. Maclean, T. H. B. Persson, M. Spitznagel, and A. García-Tabarés Valdivieso, Report from LHC MD 3312: Replicating HL-LHC DA, CERN, Geneva, Switzerland, Accelerators & Technology Sector Note CERN-ACC-NOTE-2022-0021, 2022.
- [42] W. Fischer, J. Beebe-Wang, Y. Luo, and S. Nemesure, RHIC Proton beam lifetime increase with 10- and 12-pole correctors, in *Proceedings of the International Particle Accelerator Conference, Kyoto, Japan, IPAC-2010* (BNL-90739-2010-CP, ICR, Kyoto, 2010).
- [43] H. Wiedemann, *Particle Accelerator Physics*, Graduate Texts in Physics (Springer International Publishing, Cham, 2015), 4th ed., <https://dx.doi.org/10.1007/978-3-319-18317-6>.
- [44] J. Bengtsson and J. Irwin, Analytical calculations of smear and tune shift, SSC Laboratory, Technical Report No. SSC-232, 1990.
- [45] E. H. Maclean, D. A. Wierichs, P. K. Skowronski, R. Tomás, S. Fartoukh, F. S. Carlier, and T. H. B. Persson, Demonstration of coupling correction below the Per-Mil limit in the LHC, Accelerators & Technology Sector Note CERN-ACC-NOTE-2016-0053, 2016.
- [46] E. H. Maclean, F. S. Carlier, M. Giovannozzi, T. Persson, and R. Tomás, Effect of linear coupling on nonlinear observables at the LHC, in *Proceedings of IPAC2017, Copenhagen, Denmark* (JACoW, Geneva, Switzerland, 2017), <https://dx.doi.org/10.18429/JACoW-IPAC2017-WEPIK092>.
- [47] A. Franchi, R. Tomás, and G. Vanbavinkhove, Computation of the coupling resonance driving term F1001 and the coupling coefficient C from turn-by-turn single-BPM data, CERN, Geneva, Switzerland, Accelerators & Technology Sector Note CERN-BE-Note-2010-016, 2010.
- [48] R. Tomás, Optimizing the global coupling knobs for the LHC, CERN, Geneva, Switzerland, Accelerators & Technology Sector Note CERN-ATS-Note-2012-019 MD, 2012.
- [49] T. Persson and R. Tomás, Improved control of the betatron coupling in the Large Hadron Collider, *Phys. Rev. ST Accel. Beams* **17**, 051004 (2014).
- [50] T. Persson, L. Malina, P. Skowronski, M. Gasior, R. Tomás, A. Langner, T. Lefevre, E. Maclean, J. Olexa, A. Garcia-Tabares, and J. Coello de Portugal, Experience with DOROS BPMs for coupling measurement and correction, in *Proceedings of 7th International Particle Accelerator Conference, IPAC16, Busan, Korea* (JACoW, Geneva, Switzerland, 2016), MOPMR029, <https://dx.doi.org/10.18429/JACoW-IPAC2016-MOPMR029>.
- [51] T. H. B. Persson, G. Baud, F. Carlier, J. Coello De Portugal, E. Fol, A. Garcia-Tabares Valdivieso, M. Gasior, A. Langner, E. H. Maclean, L. Malina, I. Olexa, P. K. Skowronski, R. Tomás, D. Valuch, and A. Wegscheider, Optics control in 2016, in *Proceedings of 7th Evian Workshop on LHC beam operation, Optics control in 2016, Evian Les Bains, France* (CERN, Geneva, Switzerland, 2017), pp. 77–82.
- [52] T. Persson, J. Cardona, F. Carlier, A. Costa Ojeda, J. Dilly, V. Ferrentino, E. Fol, H. García Morales, M. Hofer, E. Høydaalsvik, J. Keintzel, M. Le Garrec, E. Maclean, L. Malina, F. Soubelet, R. Tomás, A. Wegscheider, and L. Van Riesen-Haupt, Optics correction strategy for Run 3 of the LHC, in *Proceedings of 13th International Particle Accelerator Conference, IPAC22, Bangkok, Thailand* (JACoW, Geneva, Switzerland, 2022), WEPOST008, <https://dx.doi.org/10.18429/JACoW-IPAC2022-WEPOST008>.

- [53] R. J. Steinhagen, A. Boccardi, A. C. Butterworth, E. C. Giraldo, R. Denz, M. Gasior, J. L. Gonzalez, S. Jackson, L. K. Jensen, O. R. Jones, Q. King, G. Kruk, M. Lamont, S. T. Page, and J. Wenninger, Commissioning and initial performance of the LHC beam based feedback systems, in *Proceedings of the International Particle Accelerator Conference, Kyoto, Japan, 2010* (JACoW, Geneva, Switzerland, 2010), WEPEB041.
- [54] R. Steinhagen, Real-time beam control at the LHC, CERN, Geneva, Switzerland, Technical Report No. CERN-BE-2011-020, 2011.
- [55] E. H. Maclean, S. Redaelli, T. H. B. Persson, J. Uythoven, S. Moeckel, F. Schmidt, and R. Tomás, Non-linear beam dynamics tests in the LHC: LHC dynamic aperture MD on beam 2 (24th of June 2012), CERN, Accelerators & Technology Sector Note CERN-ATS-Note-2013-022 MD, 2013.
- [56] T. Bach, M. Giovannozzi, A. Langner, Y. I. Levinsen, M. Ryoichi, E. H. Maclean, M. J. McAteer, S. Redaelli, P. K. Skowronski, R. Tomás, T. H. B. Persson, and S. White, Measurement of amplitude detuning at flat-top and  $\beta^* = 0.6$  m using AC dipoles, Accelerators & Technology Sector Note CERN-ATS-Note-2013-015 MD, 2013.
- [57] R. Tomás, X. Buffat, S. White, J. Barranco, and E. H. Maclean, Collecting amplitude detuning measurements from 2012, Technical Report, 2014.
- [58] M. Bai, W. K. Van Asselt, F. Schmidt, M. Blaskiewicz, A. Lehrach, and T. Roser, Measurement of non-linearities using spectrum analysis of driven betatron oscillation, in *Proceedings of the 19th Particle Accelerator Conference, Chicago, IL, 2001* (IEEE, Piscataway, NJ, 2001), <https://dx.doi.org/10.1109/PAC.2001.987269>.
- [59] R. Tomás, M. Bai, R. Calaga, W. Fischer, A. Franchi, and G. Rumolo, Measurement of global and local resonance terms, *Phys. Rev. ST Accel. Beams* **8**, 024001 (2005).
- [60] O. E. Berrig, R. Jones, J.-P. Koutchouk, W. Höfle, J. Koopman, F. Schmidt, and H. Schmickler, Excitation of large transverse beam oscillations without emittance blow-up using the AC-dipole principle, Accelerators & Technology Sector Note CERN-SL-2001-019-BI, 2001.
- [61] O. E. Berrig, W. Höfle, R. Jones, J. Koopman, J.-P. Koutchouk, and F. Schmidt, Emittance-conserving transverse excitation using the “AC-Dipole” principle, CERN, Accelerators & Technology Sector Note SL-Note-2000-062-MD, 2004.
- [62] N. Catalan-Lasheras, S. D. Fartoukh, and J.-P. Koutchouk, Linear optics measurements using an AC-dipole excitation, CERN Technical Report No. AB-Note-2004-018, 2004.
- [63] M. Bai, S. Y. Lee, J. W. Glenn, H. Huang, L. Ratner, T. Roser, M. J. Syphers, and W. van Asselt, Experimental test of coherent betatron resonance excitations, *Phys. Rev. E* **56**, 6002 (1997).
- [64] R. Tomás, Adiabaticity of the ramping process of an ac dipole, *Phys. Rev. ST Accel. Beams* **8**, 024401 (2005).
- [65] M. Wendt, BPM Systems: A brief introduction to beam position monitoring, [arXiv:2005.14081](https://arxiv.org/abs/2005.14081).
- [66] S. Mönig, J. M. Coello de Portugal, T. Persson, A. Langner, R. Tomás, and E. Maclean, Short term dynamic aperture with AC dipoles, in *Proceedings of 7th International Particle Accelerator Conference, IPAC16, Busan, Korea* (CERN-ACC-2016-173, JACoW, Geneva, Switzerland, 2016), THPMR044, <https://dx.doi.org/10.18429/JACoW-IPAC2016-THPMR044>.
- [67] F. S. Carlier, R. Tomás, E. H. Maclean, and T. H. B. Persson, First experimental demonstration of forced dynamic aperture measurements with LHC ac dipoles, *Phys. Rev. Accel. Beams* **22**, 031002 (2019).
- [68] OMC-Team, L. Malina, J. Dilly, M. Hofer, F. Soubelet, A. Wegscheider, J. M. C. De Portugal-Martinez Vazquez, M. L. Garrec, T. Persson, J. Keintzel, H. G. Morales, and R. Tomás, OMC3, CERN, <https://dx.doi.org/10.5281/ZENODO.5705625>.
- [69] L. Malina, Novel beam-based correction and stabilisation methods for particle accelerators, Ph.D. thesis, University of Oslo, 2018.
- [70] L. Malina, Harpy: A fast, simple and accurate harmonic analysis with error propagation, in *Proceedings of the 13th International Particle Accelerator Conference, IPAC22, Bangkok, Thailand* (JACoW, Geneva, Switzerland, 2022), WEPOMS035, <https://dx.doi.org/10.18429/JACoW-IPAC2022-WEPOMS035>.
- [71] J. Dilly, Amplitude detuning—OMC documentation (2022), <https://pylhc.github.io/measurements/procedures/ampdet.html>.
- [72] A. Garcia-Tabares, F. Carlier, L. Malina, J. Coello de Portugal, A. Langner, P. Skowronski, E. Maclean, T. Persson, R. Tomás, and M. Solfaroli Camillocci, Optics-measurement-based BPM Calibration, in *Proceedings of 7th International Particle Accelerator Conference, IPAC16, Busan, Korea* (JACoW, Geneva, Switzerland, 2016), MOPMR029, <https://dx.doi.org/10.18429/JACoW-IPAC2016-THPMB041>.
- [73] A. García-Tabarés Valdivieso and R. Tomás, Optics-measurement-based beam position monitor calibrations in the LHC insertion regions, *Phys. Rev. Accel. Beams* **23**, 042801 (2020).
- [74] R. Tomás, T. Bach, R. Calaga, A. Langner, Y. I. Levinsen, E. H. Maclean, T. H. B. Persson, P. K. Skowronski, M. Strzelczyk, G. Vanbavinckhove, and R. Miyamoto, Record low beta beating in the LHC, *Phys. Rev. ST Accel. Beams* **15**, 091001 (2012).
- [75] T. Persson, F. Carlier, J. Coello de Portugal, A. G.-T. Valdivieso, A. Langner, E. H. Maclean, L. Malina, P. Skowronski, B. Salvant, R. Tomás, and A. C. G. Bonilla, LHC optics commissioning: A journey towards 1% optics control, *Phys. Rev. Accel. Beams* **20**, 061002 (2017).
- [76] A. Langner and R. Tomás, Optics measurement algorithms and error analysis for the proton energy frontier, *Phys. Rev. ST Accel. Beams* **18**, 031002 (2015).
- [77] P. T. Boggs and J. E. Rogers, Orthogonal distance regression, in *Contemporary Mathematics*, edited by P. J. Brown and W. A. Fuller (American Mathematical Society, Providence, Rhode Island, 1990), pp. 183–194, <https://dx.doi.org/10.1090/conm/112/1087109>.
- [78] R. Gommers *et al.*, SciPy: Fundamental algorithms for scientific computing in python, Zenodo, <https://dx.doi.org/10.5281/zenodo.595738>.

- [79] J. Dilly, E. H. Maclean, and R. Tomás, Controlling Landau damping via feed-down from high-order correctors in the LHC and HL-LHC, in *Proceedings of 13th International Particle Accelerator Conference, IPAC22, Bangkok, Thailand* (JACoW, Geneva, Switzerland, 2022), WEPOPT060, <https://dx.doi.org/10.18429/JACOW-IPAC2022-WEPOPT060>.
- [80] T. Gläbke, Y. I. Levinson, and K. Fuchsberger, Cpmad: Cython binding to MAD-X, <https://dx.doi.org/10.5281/zenodo.8364997>.
- [81] CERN—Accelerator Beam Physics Group, Methodical Accelerator Design—MAD-X, <http://madx.web.cern.ch/madx/>.
- [82] X. Buffat, S. Antipov, G. Arduini, R. D. Maria, N. Karastathis, S. Kostoglou, A. Koval, E. Maclean, E. Métral, N. Mounet, Y. Papaphilippou, T. Persson, and R. Tomás, Strategy for Landau damping of head-tail instabilities at top energy in the HL-LHC, CERN, Geneva, Switzerland, Accelerators & Technology Sector Note CERN-ACC-NOTE-2020-0059, 2020.
- [83] E. Forest, F. Schmidt, and E. McIntosh, Introduction to the polymorphic tracking code, SPS and LHC Division Note, CERN, Geneva, Switzerland, CERN-SL-2002-044-AP, 2002.
- [84] E. Forest, *From Tracking Code to Analysis* (Springer, Japan, Tokyo, 2016), <https://dx.doi.org/10.1007/978-4-431-55803-3>.
- [85] D. Jacquet, R. Gorbonosov, G. Kruk, and P. P. Mira, LSA—the high level application software of the LHC—and its performance during the first three years of operation, in *Proceedings of the 14th International Conference on Accelerator & Large Experimental Physics Control Systems, ICALEPCS2013* (JACoW, Geneva, Switzerland, 2014), THPPC058.
- [86] T. Persson, F. Carlier, J. Cardona, A. C. Ojeda, J. Dilly, H. G. Morales, V. Ferrentino, E. Fol, M. Hofer, E. J. Høydalsvik, J. Keintzel, M. L. Garrec, E. H. Maclean, L. Malina, F. Soubelet, R. Tomas, L. V. Riesen-Haupt, and A. Wegscheider, Linear optics measurements and corrections, CERN, LHC Machine Committee LMC No. 443, 2022.
- [87] E. H. Maclean, Non-linear optics measurements and corrections, CERN, LHC Machine Committee LMC No. 443, 2022.
- [88] J. Dilly, E. Maclean, and R. Tomás, Amplitude detuning from nonlinear-corrector- and triplet-misalignments in the LHC and HL-LHC, CERN, Geneva, Switzerland, Accelerators & Technology Sector Note CERN-ACC-2022-0078, 2022.
- [89] E. H. Maclean, Orbit at Q3 from MCSX modulation, in *Proceedings of OMC Meeting* (CERN, Geneva, 2019).
- [90] FiDeL—the magnetic model of the LHC, <https://lhc-div-mms.web.cern.ch/tests/MAG/Fidel/>.
- [91] CERN—Accelerator Technology Department, Windows interface to simulation errors, <http://wise.web.cern.ch/>.
- [92] E. Todesco, L. Bottura, M. Giovannozzi, P. Hagen, M. Juchno, M. Lamont, E. Maclean, R. T. Garcia, M. Schaumann, F. Schmidt, M. S. Camillocci, and J. Wenninger, The magnetic model of the LHC at 6.5 TeV, *IEEE Trans. Appl. Supercond.* **26**, 1 (2016).
- [93] E. H. Maclean, The B4 issue continues, in *Meeting of 3rd FiDeL Meeting Run III* (CERN, Geneva, 2020).
- [94] T. Pugnat, S. Bagnis, B. Dalena, and C. Lorin, 3D magnetic field analysis of LHC final focus quadrupoles with beam screen, in *Proceedings of IPAC'21, Campinas, Brazil* (JACoW, Geneva, Switzerland, 2021), TUPAB225, <https://dx.doi.org/10.18429/JACOW-IPAC2021-TUPAB225>.
- [95] T. Pugnat, 3D non-linear beam dynamics for the LHC upgrades, Ph.D. thesis, University Paris XI—Paris Sud, 2021.
- [96] OMC-Team and J. Dilly, IRNL RDT Correction, Zenodo, <https://doi.org/10.5281/zenodo.6373375>.
- [97] J. Dilly and R. Tomás, A flexible nonlinear resonance driving term based correction algorithm with feed-down, in *Proceedings of 13th International Particle Accelerator Conference, IPAC22, Bangkok, Thailand* (JACoW, Geneva, Switzerland, 2022), WEPOPT061, <https://dx.doi.org/10.18429/JACOW-IPAC2022-WEPOPT061>.
- [98] J. Dilly and R. Tomás, A flexible nonlinear resonance driving term based correction algorithm with feed-down, Technical Report, 2023, [https://github.com/pylhc/irnl\\_rdt\\_correction/raw/master/latex/note.pdf](https://github.com/pylhc/irnl_rdt_correction/raw/master/latex/note.pdf).
- [99] O. S. Brüning, M. Giovannozzi, S. D. Fartoukh, and T. Risselada, Dynamic aperture studies for the LHC separation dipoles, Technical Report, CERN, LHC Project Note 349, 2004.
- [100] E. H. Maclean, Modelling and correction of the non-linear transverse dynamics of the LHC from beam-based measurements, Ph.D. thesis, Herford College, University of Oxford, 2014.
- [101] J. Dilly, E. H. Maclean, and R. Tomás, Corrections of non-linear field errors With asymmetric optics in LHC and HL-LHC insertion regions, in *Proceedings of IPAC'21, Campinas, Brazil* (JACoW, Geneva, Switzerland, 2021), MOPAB258, <https://dx.doi.org/10.18429/JACOW-IPAC2021-MOPAB258>.
- [102] E. H. Maclean, J. Cardona, F. Carlier, A. C. Ojeda, J. Dilly, H. G. Morales, V. Ferrentino, E. Fol, M. Hofer, J. Keintzel, M. L. Garrec, L. Malina, T. H. B. Persson, F. Soubelet, R. Tomas, L. V. Riesen-Haupt, and A. Wegscheider, Optics commissioning, in *Proceedings of Joint Accelerator Performance Workshop* (CERN, Geneva, 2022).
- [103] E. H. Maclean, M. Giovannozzi, and R. B. Appleby, Innovative method to measure the extent of the stable phase-space region of proton synchrotrons, *Phys. Rev. Accel. Beams* **22**, 034002 (2019).